Science of the Total Environment 742 (2020) 140332

Contents lists available at ScienceDirect

Science of the Total Environment

journal homepage: www.elsevier.com/locate/scitotenv

Real-time measurement and source apportionment of elements in Delhi's atmosphere

Pragati Rai [a], Markus Furger [a,*], Imad El Haddad [a], Varun Kumar [a], Liwei Wang [a], Atinderpal Singh [b], Kuldeep Dixit [c], Deepika Bhattu [a,1], Jean-Eudes Petit [d], Dilip Ganguly [e], Neeraj Rastogi [b], Urs Baltensperger [a], Sachchida Nand Tripathi [c,*], Jay G. Slowik [a], André S.H. Prévôt [a,*]

[a] Laboratory of Atmospheric Chemistry, Paul Scherrer Institute, 5232 Villigen PSI, Switzerland
[b] Geosciences Division, Physical Research Laboratory, Ahmedabad 380009, India
[c] Department of Civil Engineering, Indian Institute of Technology Kanpur, Kanpur, Uttar Pradesh 208016, India
[d] Laboratoire des Sciences du Climat et l'Environnement, CEA/Orme des Merisiers, 91191 Gif-sur-Yvette, France
[e] Centre for Atmospheric Sciences, Indian Institute of Technology Delhi, New Delhi 110016, India

HIGHLIGHTS

- Quantified highly time-resolved elements in PM_{10} and $PM_{2.5}$ in Delhi during winters
- Source apportionment was improved combining receptor model and trajectory analysis.
- Major PM_{10} elemental constituents were Cl, S and crustal elements (Si, Ca, Ti, Fe).
- Northwest and east were the most influential source regions for various sources.

GRAPHICAL ABSTRACT

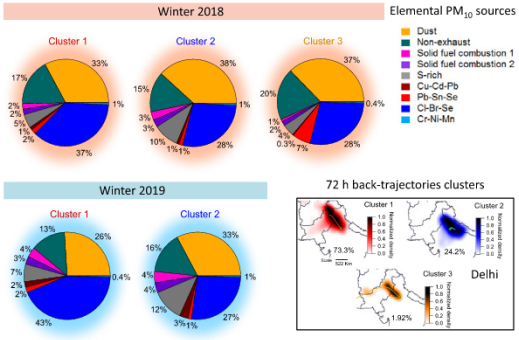

ARTICLE INFO

Article history:
Received 1 April 2020
Received in revised form 16 June 2020
Accepted 16 June 2020
Available online 23 June 2020

Editor: Pavlos Kassomenos

Keywords:
Urban air pollution
Toxic metals
Source apportionment
Industries
Non-exhaust
Local and regional source locations

ABSTRACT

Delhi, the capital of India, suffers from heavy local emissions as well as regional transport of air pollutants, resulting in severe aerosol loadings. To determine the sources of these pollutants, we have quantified the mass concentrations of 26 elements in airborne particles, measured by an online X-ray fluorescence spectrometer with time resolution between 30 min and 1 h. Measurements of PM_{10} and $PM_{2.5}$ (particulate matter <10 μm and < 2.5 μm) were conducted during two consecutive winters (2018 and 2019) in Delhi. On average, 26 elements from Al to Pb made up ~25% and ~19% of the total PM_{10} mass (271 μg m^{-3} and 300 μg m^{-3}) in 2018 and 2019, respectively. Nine different aerosol sources were identified during both winters using positive matrix factorization (PMF), including dust, non-exhaust, an S-rich factor, two solid fuel combustion (SFC) factors and four industrial/combustion factors related to plume events (Cr-Ni-Mn, Cu-Cd-Pb, Pb-Sn-Se and Cl-Br-Se). All factors were resolved in both size ranges (but varying relative concentrations), comprising the following contributions to the elemental PM_{10} mass (in % average for 2018 and 2019): Cl-Br-Se (41.5%, 36.9%), dust (27.6%, 28.7%), non-exhaust (16.2%, 13.7%), S-rich (6.9%, 9.2%), SFC1 + SFC2 (4%, 7%), Pb-Sn-Se (2.3%, 1.66%), Cu-Cd-Pb (0.67%, 2.2%) and Cr-Ni-Mn (0.57%, 0.47%). Most of these sources had the highest relative contributions during late night (22:00 local time (LT)) and early morning hours (between 03:00 to 08:00 LT), which is consistent with enhanced emissions into a shallow boundary layer. Modelling of airmass source geography revealed that the Pb-Sn-Se, Cl-Br-Se and SFC2 factors prevailed for northwest winds (Pakistan, Punjab, Haryana and Delhi), while the Cu-Cd-Pb

* Corresponding authors.
E-mail addresses: markus.furger@psi.ch (M. Furger), snt@iitk.ac.in (S.N. Tripathi), andre.prevot@psi.ch (A.S.H. Prévôt).
[1]Present address: Department of Civil and Infrastructure Engineering, Indian Institute of Technology Jodhpur, Jodhpur, Rajasthan 342037, India.

https://doi.org/10.1016/j.scitotenv.2020.140332
0048-9697/© 2020 The Authors. Published by Elsevier B.V. This is an open access article under the CC BY license (http://creativecommons.org/licenses/by/4.0/).

and S-rich factors originated from east (Nepal and Uttar Pradesh) and the Cr-Ni-Mn factor from northeast (Uttar Pradesh). In contrast, SFC1, dust and non-exhaust were not associated with any specific wind direction.
© 2020 The Authors. Published by Elsevier B.V. This is an open access article under the CC BY license (http://creativecommons.org/licenses/by/4.0/).

1. Introduction

Asia is one of the most important regions of the world in context of atmospheric aerosol loading, because of the presence of fast-growing economies such as India and China. Industrialization, urbanization, economic growth and the associated increase in energy demands have resulted in a severe deterioration of urban air quality (Li et al., 2019). The large number of pollution sources (concentrated in urban areas with dense housing, traffic and industry) may result in high pollution levels; especially if pollution controls lag behind city growth. Exposure to high pollution levels is linked to a broad spectrum of acute and chronic health effects in adults as well as children (Hooper and Kaufman, 2018). Therefore, identification of aerosol sources is a priority for assessing adequate air quality control strategies, aerosol health impacts and climate change effects. However, distinguishing between the many possible aerosol sources as well as accounting for the effects of atmospheric processing, degradation and removal processes is highly challenging. Several approaches have been used for this task, e.g. source-oriented and receptor-oriented air quality models (Amato et al., 2011; Li et al., 2012; Pant and Harrison, 2012; Belis et al., 2019; and references therein), stable and radioisotope composition of certain species (Aggarwal et al., 2013; Kirillova et al., 2014; Wang et al., 2012; Zhang et al., 2015) and chemical markers (Simoneit et al., 1999). Metals and metalloids (without accounting for C, H, N, O) have specific advantages as markers, because they persist in the atmosphere throughout the life of a particle. Most of the elements associated with fine particles are non-volatile in nature (with the notable exception of e.g. Cl), the elemental composition of particles remains unchanged even though they tend to undergo long-range atmospheric transport (Morawska and Zhang, 2002).

Certain transition metals (e.g. Fe, Cu, Mn, Zn, Ni, V, Cr, As, Pb) are emitted from a variety of sources and can have severe toxic and carcinogenic effects on humans, when inhaled in higher concentrations. Since particle size determines the rate and depth of penetration into the respiratory tract, size-resolved data is crucial for understanding and mitigating the health impacts of PM. Aerosol size distributions are governed by the physical and chemical processes contributing to their emission and atmospheric aging, and thus are source-dependent. For example, reacted Cl (inferred to be NH_4Cl) was found in $PM_{1.0–0.3}$, whereas sea/road salt related Cl resided in $PM_{10–2.5}$ (Visser et al., 2015). Similarly, K in $PM_{1.0}$ mostly originates from wood burning, but is attributed to dust in $PM_{10–1.0}$ (Viana et al., 2008).

To facilitate PM mitigation strategies, pollution sources need to be identified and apportioned. Among various receptor models, positive matrix factorization (PMF) has been developed specifically for aerosol source apportionment (SA). The PMF algorithm does not require a priori knowledge of source composition, but interpretation of the results is facilitated by information on source emission characteristics. In contrast, the chemical mass balance (CMB) receptor model, which has been used in most of the Indian SA studies so far (Gupta et al., 2007; Pipalatkar et al., 2014; Srimuruganandam and Nagendra, 2012; Thammadi et al., 2018) requires a priori knowledge of the source composition. Source profiles, resolved in PMF, may be characteristic of aged emissions, whereas those used in CMB are typically obtained from direct emission measurements, which do not consider atmospheric processing. The lack of accurate local source profiles, omission of key sources or lack of suitable markers and the need for assumptions regarding aging of the source emissions present significant challenges in the quantitative application of CMB in a complex environment. Hybrid models, implemented using the Multilinear Engine solver (ME-2) (Paatero, 1999), can combine the strengths of PMF and CMB, thus allowing for a more complete and efficient exploration of the solution space and facilitating source separation (Rai et al., 2020; Sturtz et al., 2014). In addition to source characterization, there is relatively less information available on the detailed source regions or the local/regional source contributions. Improvement can be achieved by combining source attribution and trajectory analysis.

Differences in atmospheric elemental compositions can often be observed on hourly timescales. Highly time-resolved measurements facilitate identification of point sources, which can be of specific importance in highly polluted regions with many local sources. Moreover, diurnal variations of the components, separated by PMF, are very useful for source identification. For instance, traffic emissions are expected to peak during the rush hours, while emission from domestic biomass/wood burning increase in the evening (Viana et al., 2013). While measurements of organic aerosol (OA) and major inorganic ion concentrations in fine PM are achievable on timescales of minutes using online mass spectrometry (DeCarlo et al., 2006; Fröhlich et al., 2013), elements have traditionally been measured offline. Typical sampling techniques include filter collection (Owoade et al., 2015; Tian et al., 2016) or less commonly semi-continuous samplers like streakers or rotating drum impactors (Lucarelli et al., 2018; Richard et al., 2010). However, in such semi-continuous samplers, where higher time resolution is achievable, the requirement of synchrotron light sources or other large facilities imposes practical trade-offs between time resolution, size resolution and/or temporal coverage.

Here we present semi-continuous measurements of elemental composition for $PM_{2.5}$ and PM_{10} aerosols in Delhi, India, at a time resolution of 30 min to 1 h during two consecutive winters in 2018 and 2019, to identify the prevailing sources.

2. Methods

2.1. Sampling site

National Capital Territory (NCT) Delhi is surrounded by two neighbouring states (Fig. 1), which are Uttar Pradesh to the east and Haryana in the remaining three directions. The capital of India, Delhi suffers from heavy emissions from various sources, resulting in severe PM levels (Dumka et al., 2019; Khillare and Sarkar, 2012). This city is extremely congested and overpopulated; the population of Delhi in 2011 was around 17 million and population density was 11,320 persons per km^2 (*Economic Survey of Delhi 2018–19: Planning Department, Government of NCT of Delhi*, 2019). The presence of many anthropogenic emission sources, including power plants (2 coal based, where one of them (Badarpur thermal power station) was closed on 15 October 2018 to reduce air pollution in Delhi, and 4 natural gas based), ~29 medium- and small-scale industries and 5 factory complexes (metal processing, paint, dyeing, electroplating, alloy, leather, paper, chemicals, etc.) in different industrial areas of Delhi and National Capital Region (NCR), significantly affect the air quality. Several brick kilns are also reported to operate in areas around Delhi-NCR (Guttikunda and Calori, 2013). In addition, vehicle numbers in Delhi have rapidly increased, from 3.3 million vehicles in 2000 to 11 million in 2018 (*Economic Survey of Delhi 2018–19: Planning Department, Government of NCT of Delhi*, 2019). Finally, stagnant meteorological conditions during winter trap emissions, thus producing extremely high $PM_{2.5}$ concentrations (Guttikunda and Gurjar, 2012). As a result, wintertime (December–February) has been recognized as the season with the highest concentrations of anthropogenic aerosols in Delhi (Bisht et al., 2015; Tiwari et al., 2013).

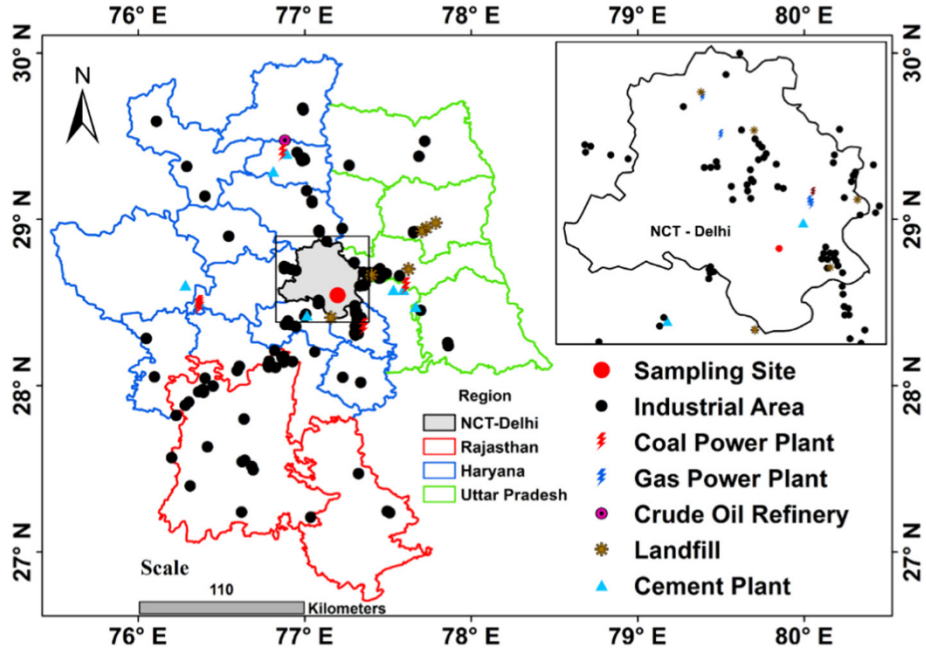

Fig. 1. The location of the study area: map of the NCT-Delhi along with nearby states (Haryana, Uttar Pradesh, Rajasthan) with various industrial areas and major industries. The site is marked as red solid point and the location of small- and medium-scale manufacturing units in the various industrial areas of Delhi is also shown (inset map on top right corner). (For interpretation of the references to colour in this figure legend, the reader is referred to the web version of this article.)

To investigate the composition of ambient air in Delhi at high time resolution, we installed a suite of semi-continuous online and online aerosol instruments at the Indian Institute of Technology Delhi (IITD) campus (28.54° N, 77.19° E) in South Delhi. The measurements were performed from 20 January until 11 March in 2018 (elemental PM_{10}, here denoted PM_{10el}) and from 15 January until 9 February in 2019 (PM_{10el} and $PM_{2.5el}$). The ambient temperature showed large variations during the 2018 campaign, with an overall increasing trend after 21 February (Wang et al., 2020). Thus, the 2018 campaign can be divided into two separate periods, comprising relatively cold (20 January–21 February) and warm (22 February–11 March) temperatures. The mean temperature (± standard deviation) measured during the cold and warm periods was 16.1 (± 5.2) °C and 23.2 (± 4.8) °C respectively, whereas it was 14.9 (± 4.3) °C in 2019. For direct comparison of ME-2 results, we also selected common (20 January–9 February) periods for both years.

The instruments were kept in a temperature-controlled laboratory on the top floor of a four-story building (~12 m high). Situated in a mixed educational, residential and commercial area, the sampling site is representative of the Delhi urban area. The nearest source of local emissions was an arterial road located 150 m away from the building. Heavy duty vehicles (HDVs) are not allowed from 07:30 to 11:00 LT and from 17:00 to 21:30 LT within Delhi, including the arterial road near the sampling site, whereas buses, light duty vehicles (LDVs) and two- and three-wheelers are not restricted (Delhi Police, 2015). It is important to note that Bharat Stage (BS) VI emission standards (equivalent to Euro 6) are applicable to the vehicles within Delhi, whereas vehicles from outside Delhi often comply with BS-IV (equivalent to Euro 4).

2.2. Instruments

Elemental composition was measured using an Xact 625i® Ambient Metals Monitor (Cooper Environmental Services, Tigard, Oregon, USA). The Xact is a sampling and analysing, non-destructive, energy-dispersive X-ray fluorescence spectrometer designed for online, semi-continuous measurements of elements in aerosols. We have modified the inlet system of the Xact to alternate between PM_{10} and $PM_{2.5}$ sampling (Furger et al., 2020) for the 2019 measurements. Because of alternating sampling, there was a gap of 30 min between each subsequent sample of the same size range. In the Xact, aerosols are sampled onto a Teflon filter tape at a flow rate of 16.7 lpm. After each sampling interval, the tape is moved forward to the analysis area, where the sample is illuminated with X-rays. The resultant excited X-ray fluorescence photons are collected with a silicon drift detector (SDD). During XRF analysis of the current sample, the next sample is collected at a clean spot on the filter tape. This cycle is repeated during each sampling interval, which was configured as 1 h in 2018 and 30 min in 2019. The obtained spectra are then analysed and calibrated online. Xact is calibrated using thin film standards for the individual elements and the response reproducibility during calibration throughout the campaign was within ±5%. Automated energy alignment checks are performed every day at midnight for 15 min, using a dynamic rod for Nb and Cr, which is inserted into the analysis area followed by a 15 min upscale check (for Cd, Cr, Nb and Pb). The same dynamic rod is also inserted into the analysis area to monitor any instability in the instrument. Thus, the sampling interval following midnight was limited to 30 min only. During our field campaigns, the hourly Nb value, which monitors the hourly XRF response, was stable within ±3%. Xact has been successfully evaluated in a number of field studies and a good agreement was found between the Xact and 24-h filter based measurements (Furger et al., 2017; Park et al., 2014; Tremper et al., 2018).

The instrument detected 35 elements (Al, Si, P, S, Cl, K, Ca, Ti, V, Cr, Mn, Fe, Co, Ni, Cu, Zn, Ga, Ge, As, Se, Br, Rb, Sr, Y, Zr, Nb, Cd, In, Sn, Sb, Ba, Hg, Tl, Pb and Bi) during the campaigns. Of these, Nb was used only for quality assurance (QA) purposes. Furthermore, some of the elements' data points were below their minimum detection limits (MDL) of the instrument (Table S1). Elements with >80% of PM_{10} and $PM_{2.5}$ data falling below the MDL were removed from further analysis (see Section 2.3).

Highly time-resolved measurements of non-refractory (NR) PM were performed using high-resolution time-of-flight aerosol mass spectrometers ($PM_{2.5}$ L-ToF-AMS in 2018 and PM_1 HR-ToF-AMS in 2019, Aerodyne Inc., USA). The different size cuts for these instruments are due to different inlet and aerodynamic lens systems. Volatile organic compounds (VOCs) were measured by a proton-transfer-reaction time-of-flight mass spectrometer (PTR-ToF-MS, Ionicon Analytical G.

m.b.H, Innsbruck, Austria) in 2018 (Wang et al., 2020) and 2019. The AMS and PTR-MS data are the focus of other studies and their data are used here for comparison with the elements' factor time series only.

NO_x was measured by chemiluminesence using a Serinus 40 Oxides of Nitrogen analyser (Ecotech). Hourly data on temperature, wind speed, wind direction, visibility and relative humidity (RH) were obtained from the Indira Gandhi International Airport (IGIA; 8 km west from our sampling site). PM_{10} and $PM_{2.5}$ mass concentrations were measured at the Rama Krishna Puram air quality monitoring station located nearby the site (~2.5 km), maintained by the Delhi Pollution Control Committee (DPCC). The mean of total PM_{10} mass during the campaigns was ~271 μg m^{-3} in 2018 (20 January–11 March) and ~300 μg m^{-3} in 2019 (15 January–9 February), whereas the mean of total $PM_{2.5}$ mass was ~180 μg m^{-3} during the 2019 campaign.

2.3. Source apportionment technique

SA of the PM_{10el} and $PM_{2.5el}$ was performed using PMF (Paatero and Tapper, 1994). PMF is a widely used algorithm for SA, which explains the variability in the elemental data (x_{ij}) as a linear combination of static factor profiles (f_{kj}) and their time dependent contributions (g_{ik}):

$$x_{ij} = \sum_{k=1}^{p} g_{ik} f_{kj} + e_{ij}, \tag{1}$$

where p is the number of factors. The indices i, j and k denote the time of measurement, element identity and factor, respectively. The elements of the model residual matrix are termed e_{ij}.

The PMF model iteratively solves Eq. (1) by minimizing the objective function (Q), which is defined as:

$$Q = \sum_i \sum_j \left(\frac{e_{ij}}{s_{ij}}\right)^2, \tag{2}$$

PMF was solved by ME-2 (Paatero, 1999 and references therein) with model configuration and post-analysis performed by the SoFi (Source Finder) Pro interface (version 6.8, PSI, Switzerland) (Canonaco et al., 2013), which is coded in the Igor Pro software environment (Wavemetrics, Inc., Portland, OR, USA). In conventional PMF analyses, rotational ambiguity coupled with limited rotational controls can impede clean factor resolution. In contrast, ME-2 provides efficient exploration of the entire solution space, by allowing the results to be directed towards environmentally meaningful solutions, implemented here by the a-value approach (Canonaco et al., 2013; Daellenbach et al., 2017; Vlachou et al., 2018). In this method, one or more factor profiles are constrained by the scalar a, which defines the allowed deviation of the retrieved factors (f_{kj}') from manually prescribed inputs (f_{kj}), according to:

$$f'_{kj} = f_{kj} \pm a \times f_{kj}, \tag{3}$$

where a can be set between 0 and 1. An a-value of 0 means no deviation is allowed, whereas 1 means 100% deviation allowed. Since factors are normalized after PMF such that the sum of each factor profile is 1, the final values of f_{kj}' may contain elements that exceed the boundaries defined by Eq. (3).

In our study, the PMF input consists of a data matrix (**X**) and an error matrix (**S**) of hourly element measurements. PMF inputs were prepared by excluding some specific elements for better source apportionment results, as outlined in the following. A common approach for the choice of species, to include in the PMF input, depends on the percentage of data below detection limit (Polissar et al., 1998). With this criterion, 24 elements (Al, Si, S, Cl, K, Ca, Ti, V, Cr, Mn, Fe, Ni, Cu, Zn, As, Se, Br, Rb, Sr, Zr, Sn, Sb, Ba and Pb) were accepted for PMF analysis. In addition, Cd and In were also included in the PMF input due to an excellent correlation between Cd—Cu and In—K during high-intensity plumes. The PMF input consists of 586 time points of 1 h each in PM_{10} during 2018 and 511 time points of 30 min in each size range (PM_{10} and $PM_{2.5}$) during 2019. The resulting 30-min factor time series of 2019 data were averaged to 1 h only for the hourly diurnal cycles. Before averaging the 30-min data points to 1 h, linear interpolation was applied between two subsequent data points for each PM size separately. We determined the PMF error matrix according to Eq. (4). For data values below MDL, x_{ij} remained unaltered while the corresponding s_{ij} was calculated using a fixed fraction of the MDL (Polissar et al., 1998) using Eq. (4). In contrast, if the concentration was greater than the MDL provided, the uncertainty was calculated using Eq. (4) (Reff et al., 2007):

$$s_{ij} = \begin{cases} \frac{5}{6} \times MDL_j, \text{if } x_{ij} < MDL_j \\ \sqrt{\left(p_j \times x_{ij}\right)^2 + \left(MDL_j\right)^2}, \text{otherwise} \end{cases} \tag{4}$$

In this study, an element specific analytical uncertainty (p_j) of 10% was used to derive the error matrix data set. The analytical uncertainty includes precision of high/medium-concentration metal standards from laboratory experiments (Phillips-Smith et al., 2017), deviation in the Nb value for each sample and deviation in the flow rate during the campaign. All the entries in x_{ij} with a signal-to-noise ratio (SNR) below 2 were down-weighted by replacing the corresponding s_{ij} with a penalty function $2/SNR_{ij}$ (Visser et al., 2015). This approach, as opposed to down-weighting an entire variable (i.e. increasing the uncertainty associated with an entire column rather than a single point (Paatero and Hopke, 2003)), allows variables with low average SNR but episodically high SNR to remain in x_{ij}, as these peaks might contain valuable information.

The availability of size segregated data allowed for several methods of constructing the input data set for ME-2 (i.e. single size × single year; single size × both years; both sizes × single year; both sizes × both years). Although all input data sets (mentioned above) were investigated separately, we found similar factor profiles and corresponding time series throughout the input data sets. Therefore, we focus our ME-2 analysis on the both sizes × both years (PM_{10el} in 2018 and $PM_{10el} + PM_{2.5el}$ in 2019) dataset. The final input matrix contained 26 variables and 1608 time points.

The exploration of the PMF solutions is thoroughly described in Section S1 in the Supplement. In brief, we considered solutions with 4 to 12 factors and selected the 9-factor solution as the best representation of the data. Factors were identified as: dust, non-exhaust, solid fuel combustion types 1 and 2 (SFC1 and SFC2), S-rich and four industrial/combustion aerosols related to plume events (Cr-Ni-Mn, Cl-Br-Se, Cu-Cd-Pb and Pb-Sn-Se). This 9-factor solution was resolved by constraining the factor profiles of SFC1, S-rich, Cu-Cd-Pb and Pb-Sn-Se, all with an a-value of 0.3. These factors were extracted beforehand from the data set by a separate unconstrained PMF (see the Supplement Section S1).

2.4. Uncertainty estimate of ME-2 results

A well-established statistical tool for estimating the uncertainty and stability of the ME-2 solution is the bootstrap technique (Brown et al., 2015; Davison and Hinkley, 1997). It consists of randomly resampling rows of the input data matrix (allowing repetitions), creating a set of new input data and error matrices with the same dimensions as the original inputs. This resampling perturbs the input data by randomly choosing rows (time points) of the original matrix, which are now present several times, while other rows are not considered (Paatero et al., 2014). We performed 1000 bootstrap runs by re-sampling rows (time of measurement) for a 9-factor solution with all factors unconstrained except for SFC1, S-rich, Cu-Cd-Pb and Pb-Sn-Se. Within the resampling operation, a-values for the constrained factors were randomly and independently initialized between 0 and 0.5 with an increment of 0.1. This kind of methodology has been adopted in previous studies

(Daellenbach et al., 2016; Stefenelli et al., 2019; Rai et al., 2020). The uncertainty estimate of ME-2 results is thoroughly described in Section S2 in the Supplement.

Overall, 991 bootstrap runs out of 1000 were classified as good or unmixed solutions (see Supplement Section S2). The average *a*-value of the constrained SFC1, S-rich, Cu-Cd-Pb and Pb-Sn-Se profiles were 0.248, 0.249, 0.252 and 0.247 respectively. The uncertainties (one σ standard deviation) of the model are shown later in Fig. 4.

2.5. Backward-trajectory (BT) clustering and concentration-weighted trajectories (CWT)

BTs show the origins of air parcels and their transport paths, and thus can provide information on the geographic location(s) of potential pollutant sources. BT analysis was done by the PC-based version of the HYSPLIT (Hybrid Single-Particle Lagrangian Integrated Trajectory, v4.1) (Draxler et al., 2018; Stein et al., 2015) model using weekly GDAS (Global Data Assimilation System) files (ftp://arlftp.arlhq.noaa.gov/pub/archives/gdas1) with a 1° × 1° resolution. The BTs were calculated for 72 h with 3 h time resolution at three different arrival altitudes (i.e. 100, 200, and 500 m) above ground level (a.g.l.). No significant differences were observed in BTs at different altitudes. The ending altitude of 100 m was selected so that the BTs ended within the mixing layer. Cluster analysis was subsequently applied to the obtained BTs to identify periods with similar geographical source regions. The optimal number of clusters was assessed from the total spatial variance (TSV) (Elbow approach) (Draxler, 1999; Syakur et al., 2018) and 3 clusters were identified. Rapid growth in TSV occurred when the number of clusters fell below 3 (Fig. S1a), therefore 3 clusters were retained as the final simulated cluster trajectories. In order to match the time resolution of BTs, all concentrations were averaged on a 3-h basis. The mean centres of cluster trajectories and occurrence of each cluster over time are represented in Fig. 3a and Fig. S1b, respectively.

We weighted the calculated BTs with the ME-2 resolved factor time series, using the CWT model (see below) to localize air parcels responsible for high measured concentrations at the receptor site (Ashbaugh et al., 1967). The factor time series were averaged to 3 h, to match the calculated BT time resolution. In this method, the average concentration-weighted trajectories are calculated as follows (Hsu et al., 2003):

$$CWT_{ij} = \frac{1}{\tau_{ij}} \sum_{k=1}^{N} C_k \tau_{ijk} \quad (5)$$

where CWT_{ij} is the average weighted concentration in the ij^{th} cell (i stands for the latitude and j for the longitude), in μg m^{-3}; k is the index of the trajectory; N is the total number of trajectories; C_k is the measured factor concentration on arrival of trajectory k, in μg m^{-3} and τ_{ijk} is the residence time of trajectory k spent within the ij^{th} cell. For BTs cluster and CWT analysis, an Igor-based user interface was used (ZeFir) (Petit et al., 2017). Endpoints at altitudes above 2000 m a.g.l. were discarded. A weighting function was added to the CWT calculation to down-weight cells associated with a low count of trajectory endpoints. The setup of the different weights is empirical, and our setup followed the recommendation of Petit et al. (2017).

3. Results and discussion

3.1. Mass concentrations and chemical composition of PM_{10el} and $PM_{2.5el}$

Temporal variations in PM_{10el} and $PM_{2.5el}$ are shown in Fig. 2 and mean values as well as average relative contributions of different elements are summarized in Tables S1 and S2, respectively, which are

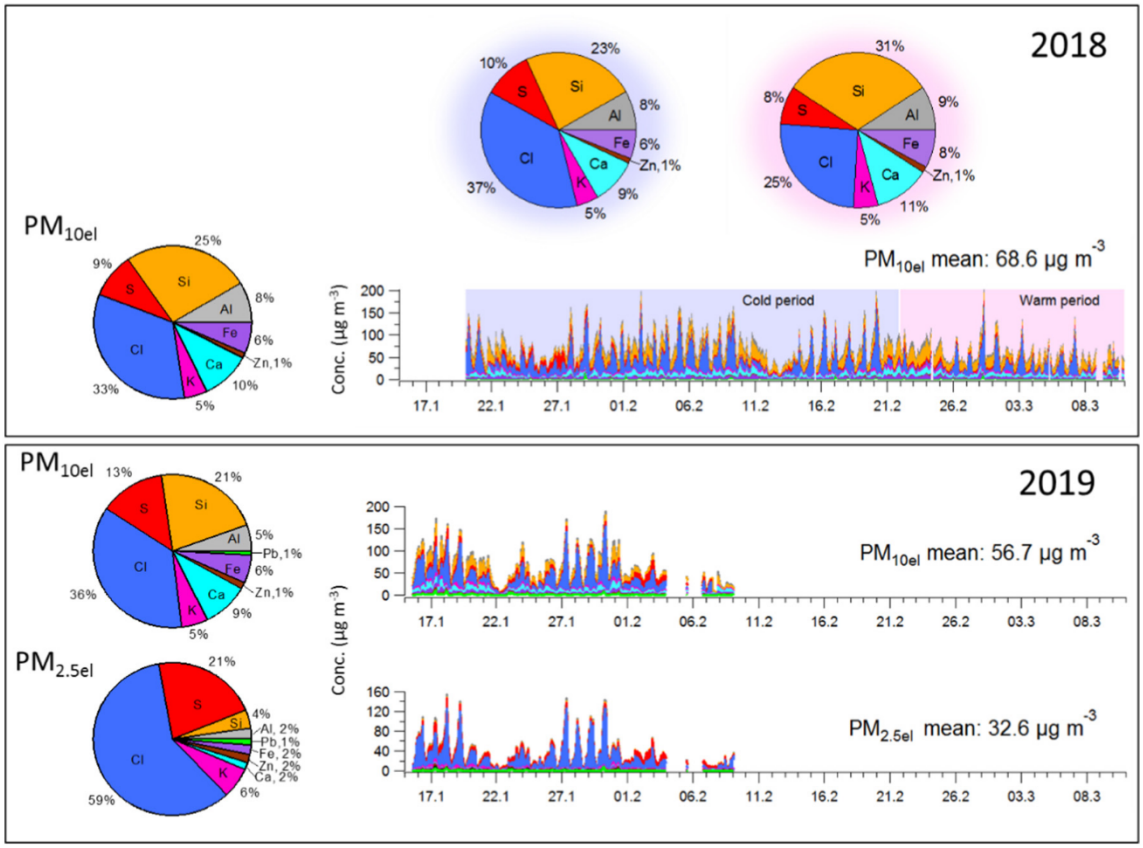

Fig. 2. Stacked time series and relative contributions (left side pie charts) of elements in PM_{10el} during 2018 (top panel) and PM_{10el}, $PM_{2.5el}$ during 2019 (lower panel). Relative contributions (top pie charts) of elements in PM_{10el} during the 2018 cold (20 January–21 February) and warm (22 February–11 March) periods. The x-axis shows the overlapping period during 2018 and 2019. Dates are dd.mm.

also reported in Fig. 2. Table S3 shows the median values and percentiles of all elements measured during both campaigns. Fig. 2 shows that Cl and Si are the predominant PM components; Cl is mainly present in $PM_{2.5el}$ while Si has high concentrations in the coarse fraction (PM_{10el}–$PM_{2.5el}$). The mean concentration of Cl and Si in PM_{10el} are higher in 2018 (22.4 μg m^{-3} and 17.4 μg m^{-3}) than 2019 (20.2 μg m^{-3} and 12.1 μg m^{-3}). Cl and Si accounted for 33% and 25%, respectively in PM_{10el} in 2018, and 36% and 21%, respectively in 2019. The relative contributions of crustal elements (Si, Ca, Ti, Fe) (see Table S2) are higher during the warm period in 2018 than the cold periods during 2018 and 2019, while this trend is reversed for Cl. The absolute concentration of Cl decreases by 42% during the warm period while there is a slight increase (2%–12%) in those of the crustal elements. Some transition metals like V and Mn in PM_{10el} exhibit higher concentrations in 2018 (8.3 ng m^{-3}, 98.8 ng m^{-3}) as compared to 2019 (5.9 ng m^{-3}, 79.3 ng m^{-3}) while it is opposite for Cu (87.3 ng m^{-3} and 128 ng m^{-3} in 2018 and 2019 respectively). Moreover, almost similar concentrations are observed for all these metals (V, Mn, Cu) during the 2018 cold and warm periods. Among the carcinogenic elements (Pb, Cr, As, Ni), Pb shows the highest mean concentrations, ranging from 421 to 498 ng m^{-3}, followed by Cr (9–42 ng m^{-3}), As (12–14 ng m^{-3}) and Ni (2–10 ng m^{-3}) in both years and in both size fractions. However, the mean concentrations of these elements (Pb, Cr, As, Ni) were below the USEPA recommended inhalation reference concentrations (RfC) for resident air (except for Pb), i.e. 200 ng m^{-3}, 100 ng m^{-3}, 15 ng m^{-3} and 20 ng m^{-3}, respectively (USEPA, 2019). Individual data points of these elements (Pb, Cr, As, Ni) exceeded the RfC values by 55.3%, 4%, 20% and 4%, respectively in 2018 and 52.8%, 0.2%, 34% and 0.4%, respectively in 2019, which indicates a potential risk to human health.

The concentration of Cl is anticorrelated with temperature, consistent with the hypothesis that the Cl-rich particles likely consist of semi-volatile species such as ammonium chloride, which evaporate with the increased temperature and decreased RH during the warmer period. Such extremely high concentrations and strong temperature-dependence have been seen for submicron Cl in other recent studies in Delhi (Bhandari et al., 2020; Gani et al., 2019). Similarly, dust resuspension is expected to increase in warmer periods due to increased temperature and wind speed coupled with decreased RH (see Fig. S2). The size-segregated data of 2019 reveals the contributions of the elements in the two size fractions. For example, the Cl contribution in PM_{10el} and $PM_{2.5el}$ is 36% and 59%, respectively while for Si it is 21% and 4%, respectively. S contributes 21% in $PM_{2.5el}$ and 13% in PM_{10el}. K presents important contributions (5–6%) in both size fractions.

The size distribution is further explored with the enrichment factor (EF) and mean ratio of $PM_{2.5el}/PM_{10el}$ (Table S4). The enrichment factor is a measure of enrichment of elements relative to the upper continental crust (UCC) and is defined as ppm metal in the sample divided by ppm metal in UCC, using Ti as reference material (Fomba et al., 2013; Majewski and Rogula-Kozlowska, 2016). The K EF ranges from 2 to 3 in PM_{10el} for both years while it is 13.7 in $PM_{2.5el}$ in 2019, with a $PM_{2.5el}/PM_{10el}$ ratio of 0.7. This indicates that K is more abundant than suggested by its crustal concentration in the fine fraction, probably from combustion (wood, coal, etc.) sources.

3.2. Geographical PM_{10el} origins

Fig. 3a shows the clustering of air mass trajectories into three footprint regions, as described in Section 2.5. Trajectories corresponding to clusters 1 and 2 are identified in both years, while cluster 3 is only found in 2018. The frequencies of the 3 clusters are 73.3%, 24.2% and ~2% respectively. Clusters 1 and 3 show air mass arrivals from the northwest at the sampling location. However, cluster 3 is driven by one specific episode from 31 January 2018 09:00 LT until 1 February 2018 15:00 LT, with a trajectory from Iran through Pakistan, Punjab and Haryana to

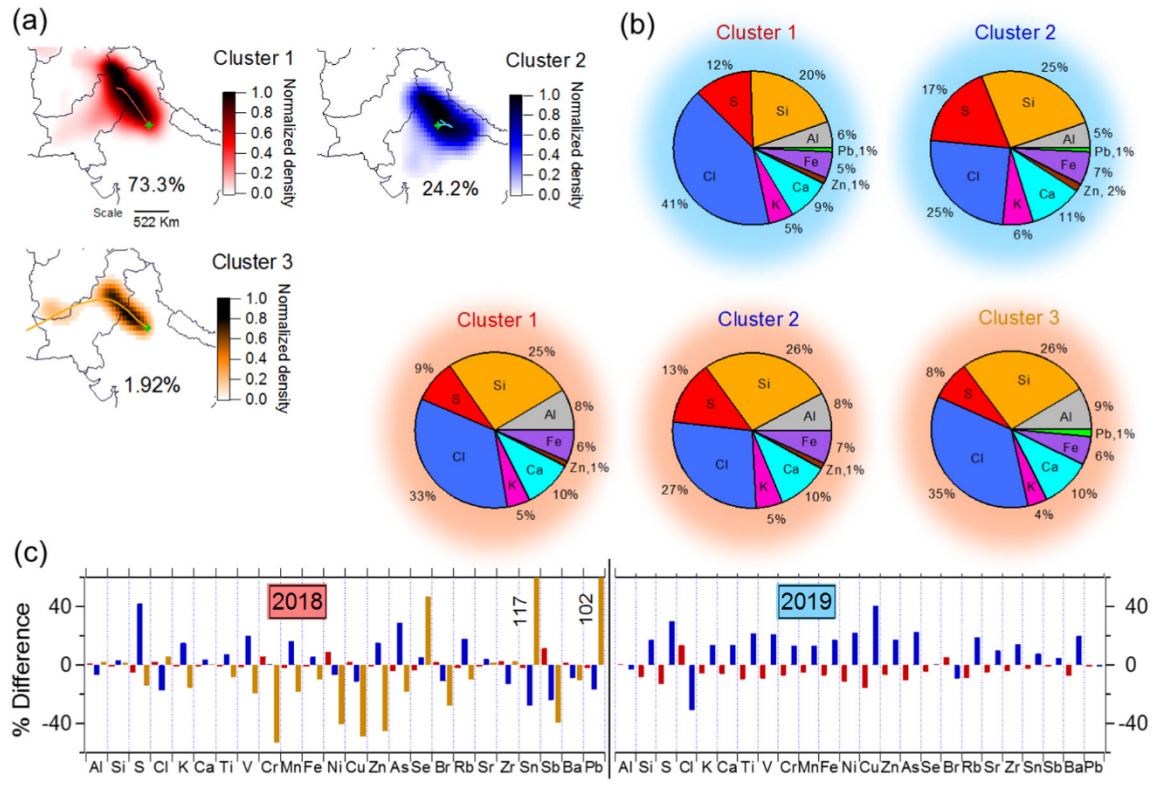

Fig. 3. (a) Heat map (density of trajectories composing each cluster where the centroid of the clusters is represented as solid line) of 72-h back-trajectories of clusters reaching the observation site (green marker) in both years including frequencies (%) of each cluster; (b) contributions of PM_{10el} in different footprint clusters in 2018 (orange pie charts) and 2019 (blue pie charts); and (c) percentage differences in the relative contributions of elements in each cluster to the total mean elemental relative contribution during 2018 (bottom left) and 2019 (bottom right). (For interpretation of the references to colour in this figure legend, the reader is referred to the web version of this article.)

the sampling site, while cluster 1 is associated with air masses travelling from the north of Pakistan to Punjab and Haryana. In contrast, cluster 2 is associated with a more local origin to the east (from Uttar Pradesh), and within Delhi.

Fig. 3b shows the elemental contributions corresponding to each cluster (pie charts). Cl is predominant with the highest concentrations for air masses from the northwest (clusters 1 and 3) which is in line with a recent study (Gani et al., 2019) during winter. It is important to note that none of clusters passes over an ocean during the 72 h prior to arriving at the site. Cl in Delhi has been linked to emissions from various industries (brick kilns, steel making, metal processing, coal power plant, etc.) (Jaiprakash et al., 2017). Therefore, we speculate that the likely sources of the measured Cl concentrations are various types of industrial emissions from Haryana, Punjab and Delhi (northwest of the sampling site) and Uttar Pradesh (east of the sampling site). S was most abundant in air masses from the east (cluster 2) in both years. These emissions might stem from coal power plants situated in the east and southeast of the sampling site.

In PM_{10el}, differences in cluster composition were further explored by calculating the percentage difference (here termed as enhancement or depletion) between the mean contribution of an element in a cluster and the total mean contribution of that respective element (Fig. 3c). Cluster 1 in 2018 does not show enhancement/depletion in any elements except for slight enhancements in Ni, Cr and Sb (up to 11%). In contrast, most of the elements are depleted (up to 20%) in cluster 1 in 2019, while Cl, Br and Al are slightly enhanced (up to 12%). Cluster 2 shows enhanced concentrations in 2018 for S, K, Ti, V, Mn, Zn, As and Rb, with the highest enhancement in S (42%). In 2019, all elements (except Cl, Br and Al) are enhanced with the maximum enhancement for Cu (40%). Cluster 3 in 2018 shows strong enhancement for Sn (117%), followed by Pb (102%) and Se (47%), while the remaining elements are depleted, especially Cr, Ni, Cu, Zn and Sb. The high deviation for some elements is driven by the concentration peaks in particular cluster. The year to year differences are visible for industrial/combustion-related elements (Cu, Pb, Sn, Se, Cr, Ni, Zn, S, As), which occur in several plume events during the measurements.

3.3. ME-2 results

As noted above, we selected a 9-factor ME-2 solution as the best representation of the data. This solution is presented in Fig. 4 (factor profiles), Fig. 5 (factor time series) and Fig. 6 (factor diurnals). These factors are interpreted as dust, non-exhaust, SFC1, SFC2, S-rich and four industrial/combustion aerosols related to plume events (Cr-Ni-Mn, Cl-Br-Se, Cu-Cd-Pb and Pb-Sn-Se). The high-time-resolution PM_{10el} SA results by ME-2 were combined with the footprint modelling (CWT and BTs clustering) to investigate the variation in source types and contributions in different source regions. Below we discuss each factor separately.

3.3.1. Dust

The dust factor accounts for >60% of Si, Ca, Ti, V and Sr, and >40% of Al, Fe and Rb. The mass of this factor (fractional composition) is dominated by Si, Ca, Fe, Al and K. These elements have been used as markers for crustal dust/soil (Sharma et al., 2016; Sun et al., 2019), consistent with the upper continental crust composition (Rudnick and Gao, 2003). This factor is predominantly found in PM_{10el} (Fig. 5) rather than $PM_{2.5el}$, indicating coarse mode particles. The absence of S in this factor profile and weak correlation between S and Ca suggests an insignificant contribution from construction activity, e.g. gypsum ($CaSO_4$). However, other kinds of construction-related dust (such as silt and gravel) are possible due to the presence of Si and Ca in the factor profile (Bernardoni et al., 2011). Therefore, this factor might not only be related to mineral soil but also to anthropogenic activities such as road dust

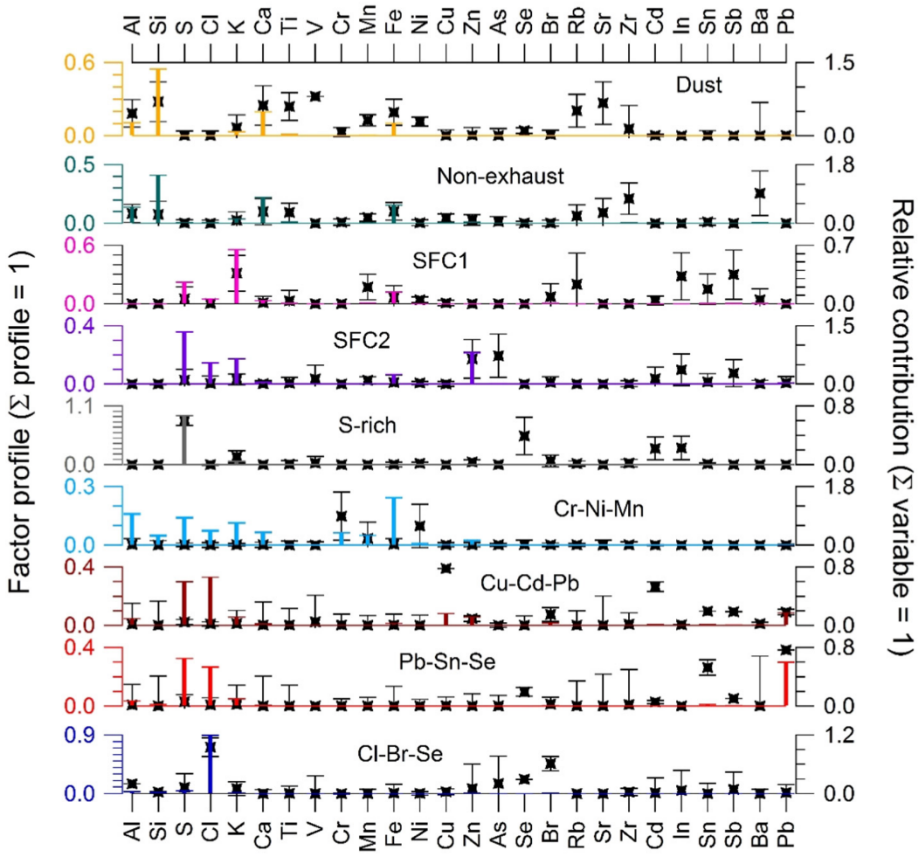

Fig. 4. Source profiles of the 9-factor PMF results. Data are given as the mean of 991 good solutions ±1 SD from the bootstrap analysis. The left axis represents the fractional composition of the factor profile (indicated as coloured bars) for each factor; the right axis represents the relative contribution of the factor to each variable (indicated as black markers).

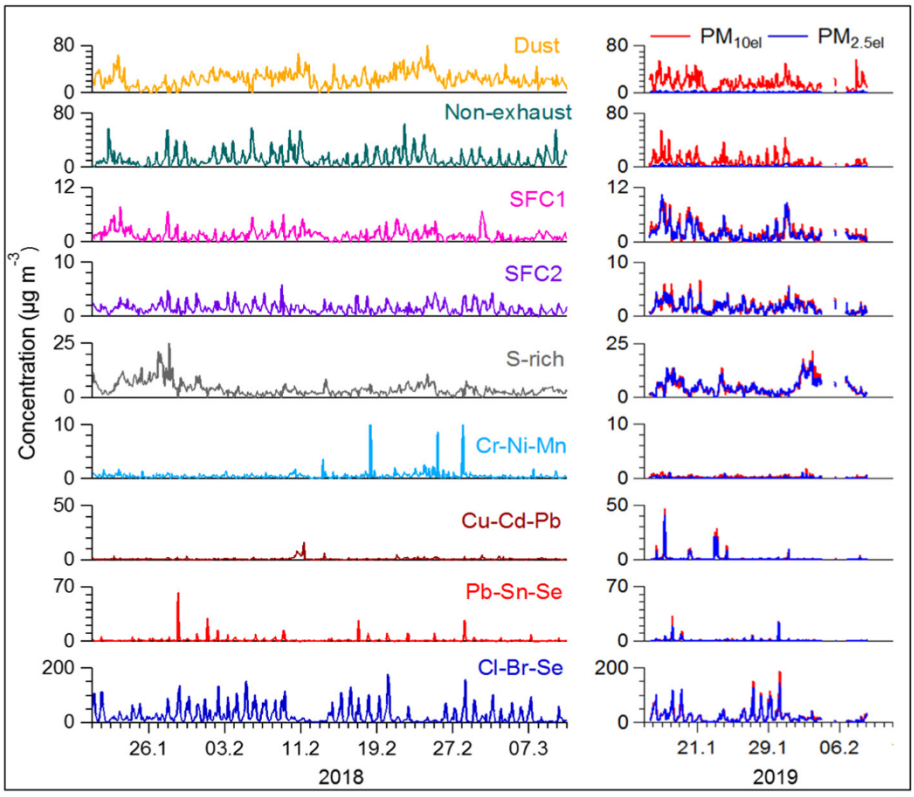

Fig. 5. Factor time series of combined ME-2 results in 2018 (left) and 2019 (right). The size-resolved factor time series (2019) are shown as PM_{10el} (red) and $PM_{2.5el}$ (blue). Dates are dd. mm. (For interpretation of the references to colour in this figure legend, the reader is referred to the web version of this article.)

resuspension, construction, demolition works and releases from buildings and other surfaces through weathering and other erosive processes. Scarce precipitation during the campaign limited the cleansing of paved surfaces and as a result, resuspension was favoured. This is further corroborated by the diurnal variations showing daytime maxima (Fig. 6a), which hints to resuspension of dust by the vehicle fleet and construction works throughout the day. The coupling of the dust factor time series with the CWT model (Fig. 7a) shows a potential source region close to the sampling site. This is distinct from the overall BT trajectory density (Fig. 7j)

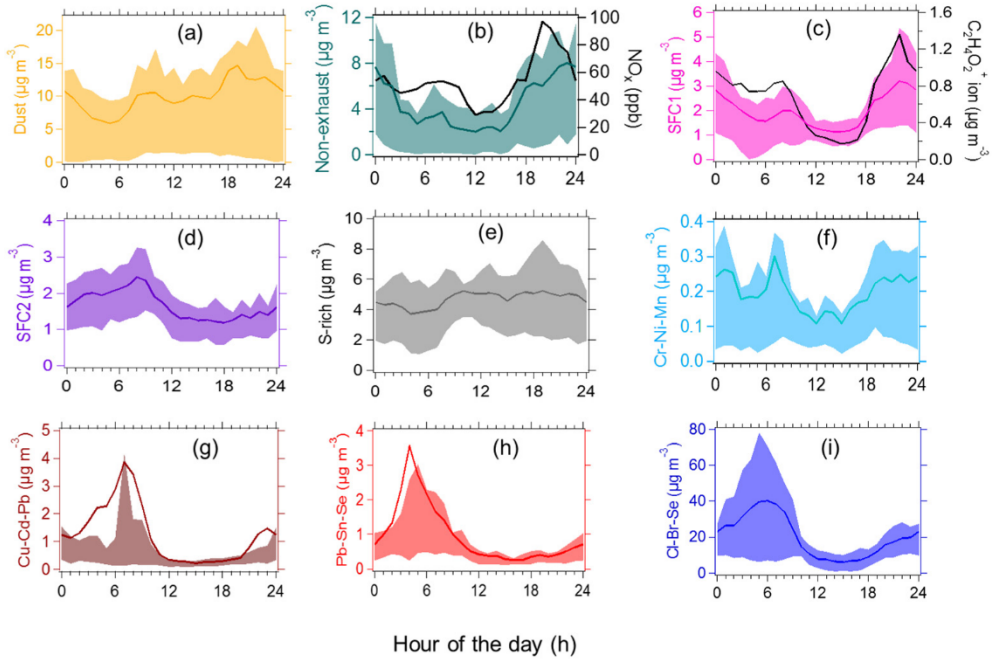

Fig. 6. Diurnal patterns, with means (coloured lines) and 25th and 75th percentiles (coloured range) of the 9 factors (a-i), along with the mean values of external data (black lines, right axis), i.e., NO_x for the brake wear factor and the $C_2H_4O_2^+$ ion for the SFC1 factor).

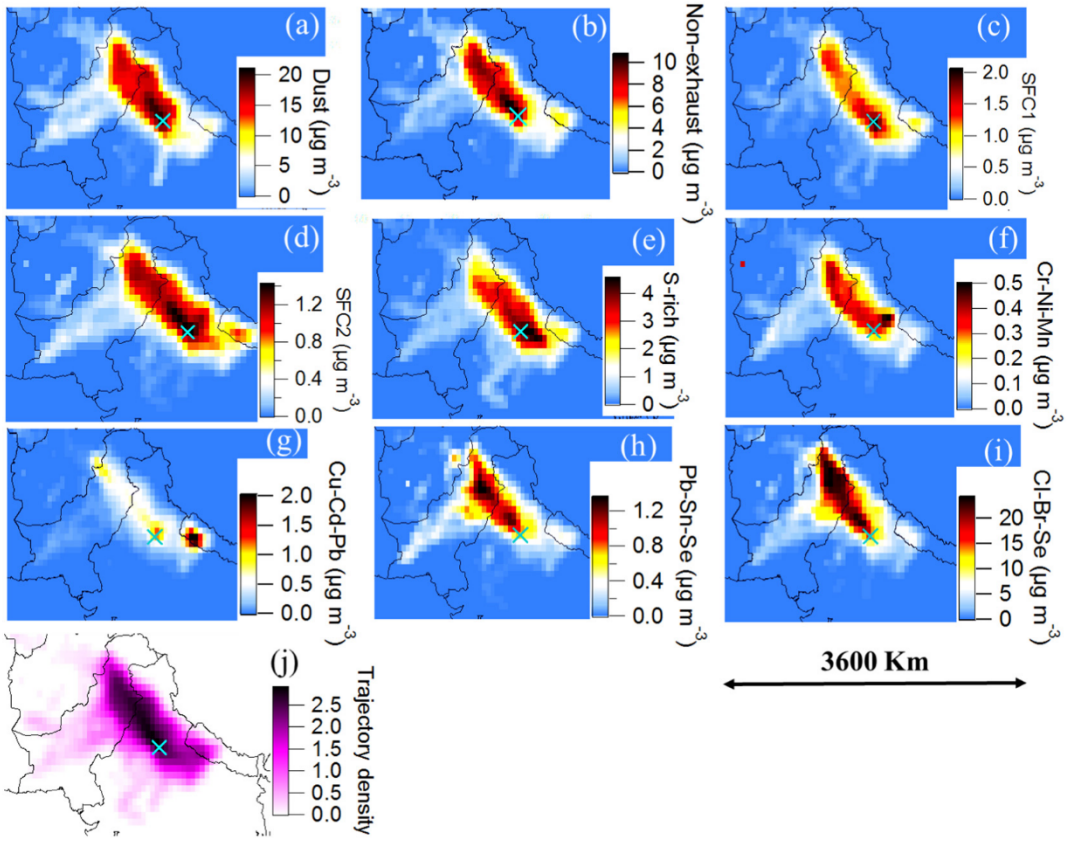

Fig. 7. CWT plots for the (a) Dust; (b) Brake wear; (c) SFC1; (d) SFC2; (e) S-rich; (f) Cr-Ni-Mn; (g) Cu-Cd-Pb; (h) Pb-Sn-Se; (i) Cl-Br-Se factors; resolved from ME-2; (j) Trajectory density, defined as $\log(N + 1)$, where N is the total number of back trajectories passing through each ij^{th} cell). The sampling location is indicated as light green cross. (For interpretation of the references to colour in this figure legend, the reader is referred to the web version of this article.)

which shows that air arrives mostly from the northwest, suggesting that the CWT result is robust.

3.3.2. Non-exhaust

This factor accounts for a dominant fraction of Ba (95%) and Zr (75%), and contributes 20–40% of Al, Si, Ca, Ti, Mn, Fe, Rb and Sr. The relative contribution to Cu is ~16%. Moreover, the mass of this factor is explained by Si (40%), Ca (22%), Fe (15%) and Al (14%). Substances such as barite ($BaSO_4$), calcite ($CaCO_3$) and mica (a silicate mineral group) are incorporated in brake lining to reduce manufacturing costs and improve manufacturability, and are used as fillers and abrasives to increase friction. Ti, Al, Sr, Mn and Rb have also been found in concentrations lower than 0.1 wt% in brake composition (Whiley, 2011). Ba comprises about 0.8% of the factor mass, similar to the reported value of 1.1% measured in London road samples (Gietl et al., 2010). Similarly, Fe accounts for ~17% of the mass, which falls in the range of 1–60% Fe in brake lining (Kennedy and Gadd, 2003). Elements such as Cu, Ba, Sb and Sn have been associated with brake wear in European studies (Bukowiecki et al., 2009; Pant and Harrison, 2013; Visser et al., 2015), but in Delhi these elements were not found to be correlated with each other. This may be due to the fact that in our study non-exhaust contributes only 16% to the total Cu, suggesting that unlike at European locations, Cu is dominated by anthropogenic sources other than non-exhaust or brake wear. The ratios of Si/Al (3), Fe/Al (1.1) and Ca/Al (1.6) found in this factor profile are in agreement with those obtained by Pant et al. (2015a) in road dust samples collected in Delhi (3.1–3.4, 0.6–1 and 1–1.6, respectively). The non-exhaust factor also contributes strongly to PM_{10el} similar to the dust factor. The diurnal pattern of this factor (Fig. 6b) corresponds to traffic rush hours (07:00–09:00 LT and 18:00–22:00 LT) and is correlated with NO_x, probably due to major traffic congestion during rush hours. Additional peaks are also observed during the night hours (between 22:00 and 03:00 LT), which might be due to enhanced heavy duty vehicular activity. The diurnal cycle of the non-exhaust factor follows the same pattern (Fig. S3) as that of hydrocarbon-like OA (HOA) from OA PMF (V. Lalchandani personal communication), as well as two traffic factors (traffic1 and traffic2, attributed to LDVs and HDVs, respectively) identified from PMF analysis of VOCs (Wang et al., 2020) in 2018. Furthermore, the time series of non-exhaust is strongly correlated with HOA ($R = 0.8$) and moderately correlated with the VOC factors corresponding to LDVs ($R = 0.67$) and HDVs ($R = 0.6$). The enhanced concentration of non-exhaust during evening rush hours is probably due to evening traffic congestion of LDVs followed immediately by night HDV activity. Additionally, it has been reported that the non-exhaust (more specifically brake wear) emission factors are higher for HDVs than for LDVs (Bukowiecki et al., 2010). The CWT plot of non-exhaust shows the highest potential source region in the northwest close to the sampling location (Fig. 7b).

3.3.3. SFC1

The SFC1 factor contributes >30% to the total of K, Sb and In, while the mass is dominated by K (51%) and S (25%). The relative contributions of this factor to Mn, As, Rb and Sn are also non-negligible (15–20%). Fine mode K and Rb are used in many SA studies as an indicator of waste incineration or coal/wood burning (Cheng et al., 2015; Tian et al., 2016; Waked et al., 2014). In addition to that K is reported to correlate ($R = 0.7$) with the oxidative potential of $PM_{2.5}$ with a probable contribution from biomass burning in Delhi during late winter 2019 (Puthussery et al., 2020). The strong correlation of this factor with the $C_2H_4O_2^+$ ion at m/z (mass to charge ratio) 60 of the AMS ($R = 0.6$–0.84), a fragment of levoglucosan, suggests primary emission

from biomass combustion (Fig. S8) (Alfarra et al., 2007). The S/K ratio of 0.5 in this factor profile is within the observed range of 0.5 (fresh emissions) to 8 (for transported/aged emissions) in solid fuel combustion-related aerosols (Viana et al., 2013) and suggests that SFC1 represents a primary aerosol. The enhancement of Sb, In, Sn, Mn and As in this factor is likely due to anthropogenic contaminants (polythene/plastic materials, foam, paper, packing materials, etc.) that are burned together with coal and/or wood. The time series of SFC1 shows concentrations up to 10 μg m^{-3}, with mass present mainly in the fine fraction. The mean concentration decreases after 25 February 2018 (from 1.6 μg m^{-3} to 1 μg m^{-3}), which is consistent with the expected decline in burning emissions during the warm period. The short-term peak on 2 March is probably due to bonfire emissions during the Holi festival. The diurnal cycles of SFC1 and the $C_2H_4O_2^+$ ion (Fig. 6c) indicate the dilution of the particles during daytime due to vertical mixing. This results in a decrease in the SFC1 concentration between 12:00 and 17:00 LT, while peaks related to residential heating/cooking activities/roadside trash burning appear in the morning (between 08:00 and 10:00 LT) and at night (with the rise starting at 18:00 LT). As already mentioned, there is a strong peak at around 22:00 LT in the SFC1 signal, which is probably related to the late-night solid fuel burning emissions in a shallower boundary layer height (BLH). The coupling of SFC1 with the CWT model (Fig. 7c) shows that this factor is dominated by local sources.

3.3.4. SFC2

SFC2 is composed mainly of Zn, S, Cl and K (26%, 26%, 24%, and 23% of the factor mass, respectively), while the relative contributions are highest for Zn (69%), As (86%), and In (38%). Co-elevated Zn and In are associated with electronic waste burning (Julander et al., 2014), whereas the combination of Zn, As, S, Cl and K is associated with coal combustion (Balakrishna et al., 2011; Chang et al., 2018). Moreover, Zn and As are also linked to iron/steel industries and waste incineration (Duan and Tan, 2013). Based on the variety of possible sources, we simply classify this factor as solid fuel combustion. Like SFC1, the SFC2 factor also occurs predominantly in fine fraction. However, there is a low correlation ($R = 0.3$) between the SFC1 and SFC2 factor time series. Other than for SFC1, the diurnal cycle for SFC2 (Fig. 6d) shows an increase in concentration from late night until the morning with the maximum at 08:00 LT, while during daytime the behaviour of SFC2 is similar to SFC1. For SFC2, the CWT (Fig. 7d) shows high concentration areas in the northwest region Punjab-Haryana, northeast region Uttar Pradesh and Delhi. This could be related to the industrial waste burning in the northwest region within Delhi and Haryana. Similar to our study, two SFC factors were also found for OA (V. Lalchandani personal communication) and VOCs (Wang et al., 2020) in 2018, although the nature of the seperation is different for each dataset. For the VOCs, SFC1 and SFC2 were attributed to primary (coal, wood and trash) and aged emissions respectively. For OA, SFC1 was characterized by burning of coal, decayed plant matter, and roadside trash, whereas SFC2 was characterized by paper and plastic burning. The correlation ($R = 0.5$–0.65) was higher among SFC1 from all three instruments (e.g. SFC1_Element vs. SFC1_VOC vs. SFC1_OA) as compared to the correlation with SFC2 from all three instruments (Fig. S4). Interestingly, the correlation is increased ($R = 0.6$–0.9) for the sum of the two SFC factors. We conclude that two SFC factors are required to represent the data variability from all three instruments; likely due to variation in emission sources as well as atmospheric reactions.

3.3.5. S-rich

The S-rich factor is nearly exclusively composed of S (92% of the factor mass), but also comprises high relative contributions to Se (38%), Cd (21%) and In (21%). Particulate S can either be directly emitted from coal combustion (Hinneburg et al., 2009) or formed through the oxidation of SO_2. The mean Se/S ratio in this factor profile (3.2×10^{-4}) is slightly lower than the Se/S ratio (4–6×10^{-4}) in coal fly ash aerosols (Chiou and Manuel, 1986). Similar to S, Se originates primarily from coal combustion and has a removal rate similar to that of sulfate; therefore, Se can be used to trace SO_2 oxidation in clouds and fog (Husain et al., 2004). The presence of Se in the S-rich factor is consistent with the findings of previous studies (Hao et al., 2020; Weber et al., 2019). Cd and In are tracers for coal fly ash from coal power plants (Chakraborty and Gupta, 2010; Gollakota et al., 2019; White and Hemond, 2019). The S-rich factor shows a strong correlation with AMS sulfate (Fig. S8) and is interpreted to be related to secondary aerosol from coal combustion (Sharma et al., 2014). The S-rich factor is predominantly found in the fine fraction. In addition, this factor shows enhanced concentrations during cold periods, probably due to stagnant ambient air with little vertical dilution. The diurnal pattern of this factor is flat (Fig. 6e), in contrast to the primary emissions discussed above (Dust, Non-exhaust, SFC1 and SFC2), suggesting a more regional source character. Taken together, this evidence suggests that the S-rich factor represents primary, secondary and aged aerosols. The CWT plot for the S-rich factor (Fig. 7e) likewise suggests advection from nearby cities. The highest concentrations for the S-rich factor are found for east and southeast directions. The local power plants Badarpur in the southeast (~17 km away from the sampling location) within Delhi, Aligarh in the southeast (~160 km) in Uttar Pradesh, and Dadari in the east (~68 km) in Uttar Pradesh of the receptor site are probable contributors of coal-related primary particles and precursors for secondary aerosol.

3.3.6. Anthropogenic industrial/combustion plume events (Cr-Ni-Mn, Cu-Cd-Pb, Pb-Sn-Se and Cl-Br-Se)

Four anthropogenic factors (Cr-Ni-Mn, Cu-Cd-Pb, Pb-Sn-Se and Cl-Br-Se), most likely from industry and/or combustion emissions, were resolved. All of them yielded episodic plume events in the factor time series with the exception of the Cl-Br-Se factor, which showed regular and strong peaks at ~06:00 LT every day.

As a complement to the PMF analysis, *k*-means clustering analysis was applied to the measured time series (see details in Supplement Section S3). This analysis yielded 4 clusters corresponding to spikes in the concentrations of one or more elements. The time series of these plume-driven factors were comparable to those of the anthropogenic industrial/combustion plume factors retrieved from PMF. The agreement between these two independent analyses supports both the robustness of the retrieved PMF factor profiles and time series, as well as the interpretation of these signatures as being characteristic of specific plumes. The characteristic features of these 4 factors are discussed below.

The Cr-Ni-Mn factor profile contains high relative contributions for Cr (98%), Ni (64%) and Mn (20%). However, Fe (25%), Al (19%) and S (16%) dominate the mass. The former elements (Cr, Ni and Mn) have been associated with various emission sources in previous studies, such as traffic-related, industrial activities, waste incineration, solid waste dumping and oil combustion (Khillare and Sarkar, 2012; Matawle et al., 2015; Pant and Harrison, 2012). Ni may come from the burning of lubricating oil and heavy fuel oil used in industries and ships. Mn is used as an additive in vehicular fuel, while Cr and Ni may be derived from vehicle fuel combustion processes (Karar et al., 2006; Ntziachristos et al., 2007; Song and Gao, 2011). The low mass fraction (~1%) of Ni is in agreement with 0.5–1% of Ni in a gasoline exhaust factor profile obtained by Srimuruganandam and Nagendra (2012) at a busy roadside in Chennai, India. Cr and Ni show spiky time series in our study. As a result, a spiky factor time series is resolved by PMF in both sizes (PM_{10} and $PM_{2.5}$), which is a typical indication for influences of one or more point sources close to the sampling site. Moreover, the strong correlation between Cr and Ni ($R = 0.97$) and their weak correlation with the remaining elements during these spikes suggests different emission sources than for the other elements. However, the correlations of Cr and Ni with the non-exhaust -related elements (Ba, Zr, Al, Si, Ca, Ti, Mn, Fe, Rb and Sr) as well as with the non-exhaust factor time series are rather high ($R = 0.55$–0.75) during non-spiky periods.

These systematic compositional differences between spike-plume and non-spike-plume periods suggest that the spike-plumes originate from non-traffic-related sources. The similarity of the diurnal pattern of the Cr-Ni-Mn factor (Fig. 6f) with the non-exhaust factor is in agreement with the traffic influence. In 2018, more high intensity plumes were observed as compared to 2019 (Fig. 5). Trajectory analysis (Fig. 7f) suggests Uttar Pradesh and Uttarakhand (east-northeast) as a likely source region for these emissions.

The Cu-Cd-Pb factor profile shows high relative contributions of Cu (78%), Cd (53%) and Pb (19%), plus non-negligible contributions of Sn (19%), Sb (18%) and Br (15%). However, Cl (33%) and S (30%) dominate the mass. The elements in this factor profile are associated with various types of industrial activities. For example, Cu and Cd have been found from Cu—Cd alloy manufacture (Vincent and Passant, 2006), whereas Cu and Pb from industrial metal and lead-acid battery production/recycling (Jaiprakash et al., 2018). The elements in this factor profile are also associated with electrical/electronic equipment waste burning with high loading of Cu (Frazzoli et al., 2010; Owoade et al., 2015; Wong et al., 2007). This may be likely due to the fact that Cu is one of the extensively used materials in electric and electronic equipment because of its excellent conductivity. Other elements in this factor indicate a mixture of waste materials such as printed circuit boards (Cu, Cd, Pb, Sn, Sb), cables (Cu), plastic chips (Cd), solder (Pb, Sn), LCD monitors (Pb, Sn), etc. This factor is predominantly in the fine fraction and the time series shows several episodic plumes throughout the measurements (especially in 2019) (Fig. 5); with the concentrations ranging from 3.5 μg m^{-3} to 47 μg m^{-3}. Most of these high-intensity plumes appear at ~07:00 LT (Fig. 6g). Overall, this factor is likely to be influenced by various types of industrial and/or electronic waste burning events. The Cu-Cd-Pb factor shows high concentrations originating from the area bordering India and Nepal (Fig. 7g) as well as close to Delhi. In India, there are numerous sites known for the informal recycling or recovery of valuable materials from electronic waste. The main centre, where most of the informal recycling is performed via open burning of electronic waste, is Moradabad (east-northeast ~200 km from the sampling site).

The Pb-Sn-Se factor profile shows high relative contributions of Pb (78%), Sn (54%) and Se (19%), whereas the mass is dominated by S (37%), Pb (33%) and Cl (20%). Pb and Sn have been used as tracers for open waste/plastic burning (Kumar et al., 2015; Kumar et al., 2018), as well as from lead smelting (Jaiprakash et al., 2017; Patil et al., 2013). Pb is strongly enhanced in lead smelting emissions (Patil et al., 2013). Recovery of lead from used car batteries is a common practise in Delhi-NCR small-scale industrial areas, which are mainly in the northwest and southeast of the sampling site. Note that while Pb and Sn may be emitted from brake wear (Bukowiecki et al., 2009) and waste incineration, the absence of traffic rush hour peaks in the diurnal cycle for these two elements makes a strong vehicular source unlikely. In addition, Pb from exhaust emission is very unlikely due to the ban of leaded fuel in India since 2000. Similar to the Cu-Cd-Pb factor, this factor also predominates in the fine fraction with several episodic plumes. Although the frequency of plumes is comparable in both years, the plume concentrations are strongly enhanced in 2018 (Fig. 5). The diurnal pattern of this factor shows enhanced concentration from 03:00 until 08:00 LT (Fig. 6h) probably due to the shallow BLH in the early morning. Higher Pb concentrations are observed during night time as compared to day time. This observation is in agreement with a previous study (Chandra et al., 2014), where the highest Pb concentrations were found during night time throughout the year. However, they reported 12-h Pb air samples measurements which prevented identification of the plume-dominated temporal characteristics of Pb. The potential source region of this factor indicates the dominance in the northwest, mainly from the northeast part of Pakistan, Punjab and Haryana (Fig. 7h). A very similar potential source region for Pb has been reported by Chandra et al. (2014).

The Cl-Br-Se factor profile shows high relative contributions for Cl (95%), Br (62%), Se (32%) and Al (20%), while the mass is mainly composed of Cl (89%) and predominantly found in the fine fraction. While Cl, Br, Se, and Al originate from a variety of sources, Al is not correlated with dust-related elements in the fine fraction but instead with Cl ($R = 0.84$) and Br ($R = 0.78$). This suggests co-emission of these elements, likely from metallurgical/chemical industries, coal combustion and trash burning. Br has been reported from wood combustion, waste incineration and traffic emissions from fuel additives (Khodeir et al., 2012). The Cl-Br-Se factor shows enhanced concentrations from midnight until 08:00 LT (Fig. 6i), however, as this diurnal pattern is mostly driven by the ambient temperature and the shallow BLH, due to the semi-volatile nature of its main components, no source information can be retrieved from it.

In winter, brick kilns are reported to operate in areas surrounding Delhi, and can contribute to high Cl concentrations. Around 1000 brick kilns are located mostly along the border of Delhi in all directions, with a production capacity of 25,000 bricks per day. Bricks are typically baked in traditional kilns that burn coal and biomass, which could emit Se, Cl and Br, whereas Al is contained in the clay for the brick material. Direct Cl emissions are also possible in the form of HCl from industries like steel making, where HCl is used during the pickling process of hot and cold rolling of steel sheets. Br and Se in the fine fraction are possible from various drug and chemical manufacturing industries, as reported in a previous study in Mumbai, India (Kothai et al., 2011). However, most of the drug manufacturing industries are mainly in Gujarat and Mumbai.

Cl is also found to be emitted from garbage burning worldwide (Dall'Osto et al., 2013; Jayarathne et al., 2018; Li et al., 2012). Li et al. (2012) reported up to 3 ppb HCl in Mexico City, suggesting garbage burning as a major source (up to 60%) of particulate chloride. Delhi is an ammonia rich environment (Van Damme et al., 2018; Warner et al., 2017) and most of the chlorine is present in the form of ammonium chloride (Pant et al., 2015b) during winter. Along with the emission sources, low temperature, high RH and a shallow BLH during winter support the enhancement in Cl concentrations (Pant et al., 2015b).

Overall, this factor is likely influenced by several industrial emissions such as brick kilns, steel making, chemical manufacturing and garbage/coal burning. The CWT plots (Fig. 7i) for the Cl-Br-Se factor show high concentrations in the northwest, with air masses travelling over Pakistan, Punjab and Haryana contributing to this factor. Bhandari et al. (2020) also reported an ammonium chloride factor resolved from PMF on an aerosol chemical speciation monitor (ACSM), with 87% of the factor contribution from the northwest direction at the same sampling location.

3.4. Synthesis of ME-2 results

The elemental SA results indicate the ability to characterize the environment-dependent variability of emissions in and around Delhi. The averaged relative contributions of the factors and the stacked factor time series in both years are shown in Fig. 8 and Fig. S5, respectively. The elemental mass was calculated as the sum of all elemental species in each factor. The mass of the total PM_{10el} is dominated by the Cl-Br-Se factor, followed by the dust, non-exhaust and S-rich factors in both years (Fig. 8). The mass of total $PM_{2.5el}$ is strongly driven by Cl-Br-Se followed by the S-rich and the two SFC factors, while the dust and non-exhaust factors show lower contributions (~9 times and ~4.7 times lower, respectively) than to total PM_{10el}. Similarly, Cu-Cd-Pb and Pb-Sn-Se showed higher relative contributions in $PM_{2.5el}$, while the Cr-Ni-Mn factor was attributed in both sizes.

ME-2 results coupled with BT clustering analysis are shown in Fig. 8. Relatively high contributions of the Cl-Br-Se factor were observed (27%–43%) from all footprint regions, with the highest from the northwest (cluster 1: 2018: 37% and 2019: 43%). In contrast, the contributions of

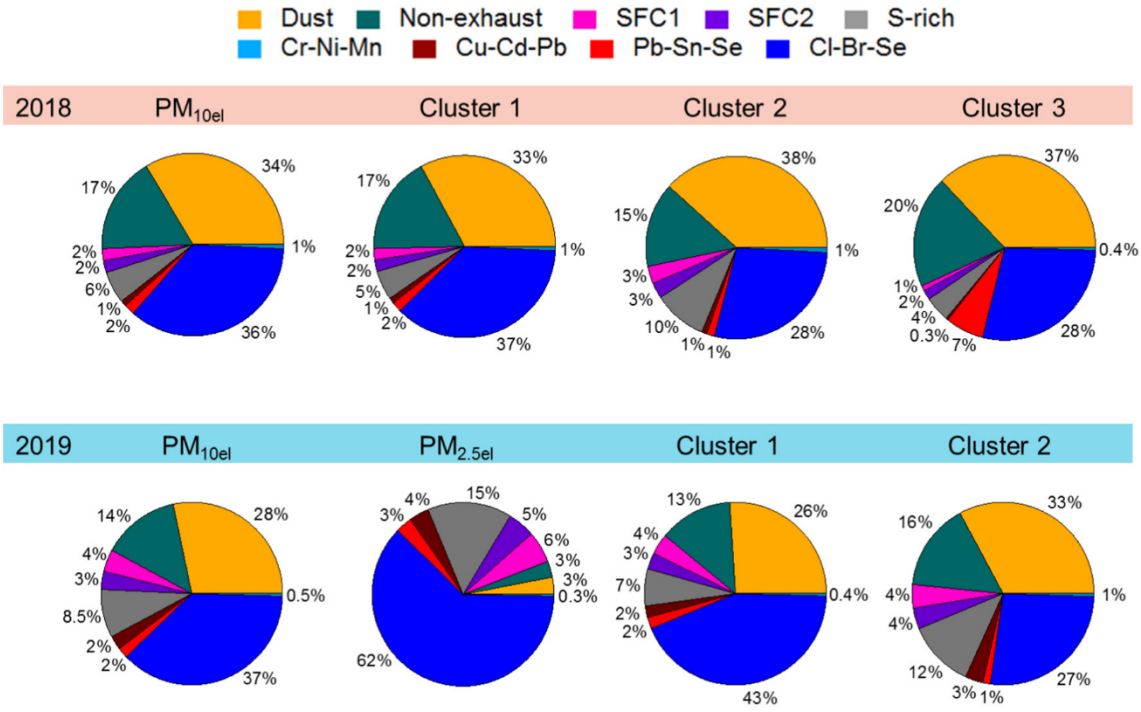

Fig. 8. Average relative source contributions of PM_{10el} for the entire 2018 period and for 3 separate clusters during 2018 (top pie charts); average relative source contributions of PM_{10el} and $PM_{2.5el}$ for the entire 2019 period and for 2 clusters during 2019 (lower pie charts).

the dust and S-rich factors were most significant from the east (cluster 2: 2018: 38%, 10% and 2019: 33%, 12% respectively). Moreover, it is interesting to note that the contribution of the Pb-Sn-Se factor was higher (7%) from the northwest (cluster 3). The Cu-Cd-Pb factor contribution was highest (3%) from the east during 2019, while in 2018 it was relatively similar (1%) from both regions (cluster 1 and cluster 2) with negligible contribution (0.3%) in cluster 3. The Cr-Ni-Mn factor showed similar contributions (1%) from the northwest and the east (cluster 1 and cluster 2) in 2018, whereas it was dominant from the east (cluster 2) in 2019.

Cl-Br-Se, dust, non-exhaust, S-rich, Pb-Sn-Se and Cr-Ni-Mn showed significantly higher concentrations in 2018, while SFC1 and SFC2 were similar in both years (Fig. 9a). Interestingly, the Cu-Cd-Pb factor was the only factor to show significant enhancement in 2019. In terms of relative contribution (Fig. 9b), dust (28.7%), SFC1 (3.6%), SFC2 (3.4%), S-rich (9.2%) and Cu-Cd-Pb (2.2%) were higher in 2019 compared to

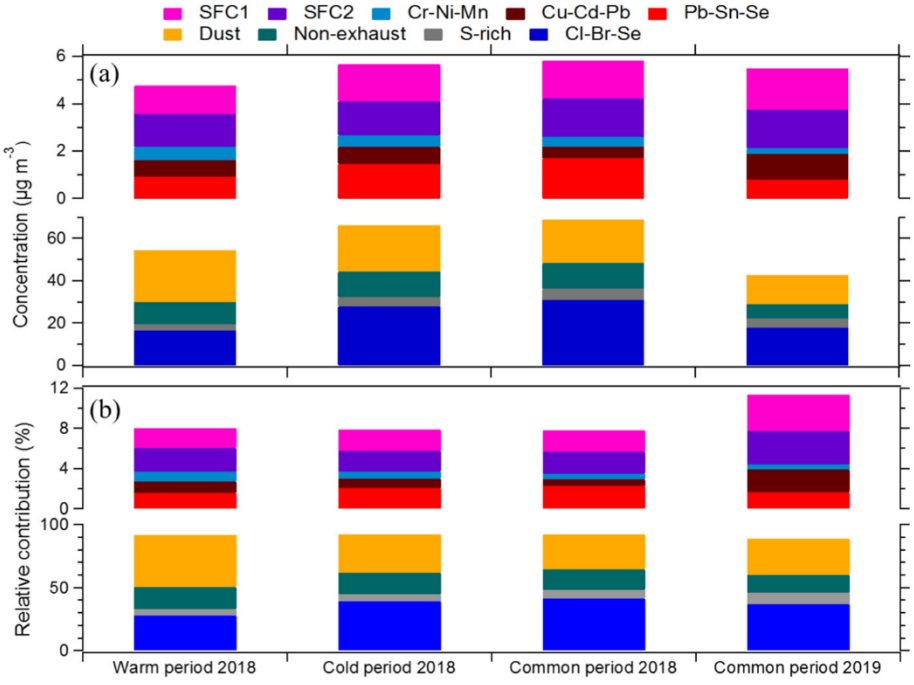

Fig. 9. Comparison of the 9 factors: (a) mean concentrations and (b) relative contributions in PM_{10el} during the warm period (22 February–11 March) 2018, the cold period (20 January–21 February) 2018 and the common periods (20 January–9 February) in both years.

2018 (27.6%, 2%, 2%, 6.9%, 0.7% respectively). Furthermore, the dust factor showed a higher contribution (41%), while the Cl-Br-Se and Pb-Sn-Se factors showed lower contributions during the warm period compared to the cold period. This shows the significant influence of temperature on the source concentration enhancement/depletion.

4. Conclusions

Source apportionment was performed on size-resolved, online PM_{el} measurements by an Xact 625i in Delhi during two consecutive winters (2018 and 2019). Elements measured by the Xact represent ~25% in 2018 and ~ 19% in 2019 of total PM_{10}, with the dominant elements consisting of Cl, S and crustal material (i.e., Si, Ca, Ti, Fe). This provides insight into key PM sources in Delhi such as dust, inorganic constituents e.g. chloride, and public health risks due to the extremely high concentrations of carcinogenic (Cr, Ni, As, Pb) and other elements (Cl, Zn, Cu, Mn, V, etc.).

The ME-2 analysis of the combined data yielded 9 source profiles, allowing for a direct comparison of the source strengths over two consecutive winters. The size-segregated SA results highlight that dust and non-exhaust sources strongly contributed to PM_{10el}, while the remaining factors (except Cr-Ni-Mn) were mostly associated with $PM_{2.5el}$. Furthermore, the elemental composition and SA results in the cold and warm periods revealed that the concentrations for the Cl-Br-Se and Pb-Sn-Se factors decreased with increasing temperature and wind speed and decreasing RH. In contrast, there was a strong enhancement in the dust factor during the warm period, consistent with resuspension with dry ambient conditions.

A clear advantage of a high time resolution elemental dataset is the possibility to enable diurnal patterns as well as plume characterization of emission sources. This is particularly important for aerosol sources observed primarily from diffuse local emissions (e.g. traffic) as well as discrete plumes (typically lasting at most a few hours) as a function of time of day rather than regional contributions. To assess the geographical origins of the resolved sources, ME-2 results were combined with a BT cluster footprint model and a CWT model, to analyse the specific sources from different regions around Delhi. The Cl-Br-Se source was predominantly from the northwest and likely influenced by regional (from Punjab and Haryana) as well as local sources (within Delhi). Dust, non-exhaust and SFC1 were classified as being of local origin. The S-rich and Cr-Ni-Mn factors likely originated in Uttar Pradesh (northeast to southeast), the Cu-Cd-Pb factor from Nepal and Uttar Pradesh (east), while Pb-Sn-Se and SFC2 originated in Haryana, Punjab and Pakistan (northwest). Overall, the ME-2 receptor modelling applied to the hourly resolution and size-segregated elemental concentrations obtained by the Xact has proven useful in identifying different regional and local aerosol sources as well as different types of industrial/combustion plume events.

Data availability

Data related to this article are available at https://doi.org/10.5281/zenodo.3907250.

Declaration of competing interest

The authors declare that they have no known competing financial interests or personal relationships that could have appeared to influence the work reported in this paper.

Acknowledgments

This study has been funded by the Swiss National Science Foundation (SNSF grants 200021_162448, 200021_169787 and BSSGI0_155846), and by the Federal Office for the Environment (FOEN). S. N. Tripathi was financially supported by the Department of Biotechnology (DBT), Government of India under grant no. BT/IN/UK/APHH/41/KB/2016-17 and by Central Pollution Control Board (CPCB), Government of India under grant no. AQM/Source apportionment EPC Project/2017. All co-authors gratefully acknowledge their support, which has helped in conducting this research.

Appendix A. Supplementary data

Supplementary data to this article can be found online at https://doi.org/10.1016/j.scitotenv.2020.140332.

References

Aggarwal, S.G., Kawamura, K., Umarji, G.S., Tachibana, E., Patil, R.S., Gupta, P.K., 2013. Organic and inorganic markers and stable C-, N-isotopic compositions of tropical coastal aerosols from megacity Mumbai: sources of organic aerosols and atmospheric processing. Atmos. Chem. Phys. 13, 4667–4680. https://doi.org/10.5194/acp-13-4667-2013.

Alfarra, M.R., Prévôt, A.S.H., Szidat, S., Sandradewi, J., Weimer, S., Schreiber, D., Mohr, M., Baltensperger, U., 2007. Identification of the mass spectral signature of organic aerosols from wood burning emissions. Environ. Sci. Technol. 41, 5770–5777. https://doi.org/10.1021/es062289b.

Amato, F., Pandolfi, M., Moreno, T., Furger, M., Pey, J., Alastuey, A., Bukowiecki, N., Prévôt, A.S.H., Baltensperger, U., Querol, X., 2011. Sources and variability of inhalable road dust particles in three European cities. Atmos. Environ. 45, 6777–6787. https://doi.org/10.1016/j.atmosenv.2011.06.003.

Ashbaugh, L.L., Malm, W.C., Sadeh, W.Z., 1967. A residence time probability analysis of sulfur concentration at Grand Canyon National Park. Atmos. Environ. 19, 1263–1270. https://doi.org/10.1016/0004-6981(85)90256-2.

Balakrishna, G., Pervez, S., Bisht, D.S., 2011. Source apportionment of arsenic in atmospheric dust fall out in an urban residential area, Raipur, central India. Atmos. Chem. Phys. 11, 5141–5151. https://doi.org/10.5194/acp-11-5141-2011.

Belis, C.A., Favez, O., Mircea, M., Diapouli, E., Manousakas, M.-I., Vratolis, S., Gilardoni, S., Paglione, M., Decesari, S., Mocnik, G., Mooibroek, D., Salvador, P., Takahama, S., Vecchi, R., Paatero, P., 2019. European Guide on Air Pollution Source Apportionment With Receptor Models – Revised Version 2019. JRC117306. EUR. 29816. EN, Publications Office of the European Union, Luxembourg. https://doi.org/10.2760/439106.

Bernardoni, V., Vecchi, R., Valli, G., Piazzalunga, A., Fermo, P., 2011. PM_{10} source apportionment in Milan (Italy) using time-resolved data. Sci. Total Environ. 409, 4788–4795. https://doi.org/10.1016/j.scitotenv.2011.07.048.

Bhandari, S., Gani, S., Patel, K., Wang, D.S., Soni, P., Arub, Z., Habib, G., Apte, J.S., Hildebrandt Ruiz, L., 2020. Sources and atmospheric dynamics of organic aerosol in New Delhi, India: insights from receptor modeling. Atmos. Chem. Phys. 20, 735–752. https://doi.org/10.5194/acp-20-735-2020.

Bisht, D.S., Dumka, U.C., Kaskaoutis, D.G., Pipal, A.S., Srivastava, A.K., Soni, V.K., Attri, S.D., Sateesh, M., Tiwari, S., 2015. Carbonaceous aerosols and pollutants over Delhi urban environment: temporal evolution, source apportionment and radiative forcing. Sci. Total Environ. 521–522, 431–445. https://doi.org/10.1016/j.scitotenv.2015.03.083.

Brown, S.G., Eberly, S., Paatero, P., Norris, G.A., 2015. Methods for estimating uncertainty in PMF solutions: examples with ambient air and water quality data and guidance on reporting PMF results. Sci. Total Environ. 518–519, 626–635. https://doi.org/10.1016/j.scitotenv.2015.01.022.

Bukowiecki, N., Lienemann, P., Hill, M., Figi, R., Richard, A., Furger, M., Rickers, K., Falkenberg, G., Zhao, Y., Cliff, S.S., Prévôt, A.S.H., Baltensperger, U., Buchmann, B., Gehrig, R., 2009. Real-world emission factors for antimony and other brake wear related trace elements: size-segregated values for light and heavy duty vehicles. Environ. Sci. Technol. 43, 8072–8078. https://doi.org/10.1021/es9006096.

Bukowiecki, N., Lienemann, P., Hill, M., Furger, M., Richard, A., Amato, F., Prévôt, A.S.H., Baltensperger, U., Buchmann, B., Gehrig, R., 2010. PM_{10} emission factors for non-exhaust particles generated by road traffic in an urban street canyon and along a freeway in Switzerland. Atmos. Environ. 44, 2330–2340. https://doi.org/10.1016/j.atmosenv.2010.03.039.

Canonaco, F., Crippa, M., Slowik, J.G., Baltensperger, U., Prévôt, A.S.H., 2013. SoFi, an IGOR-based interface for the efficient use of the generalized multilinear engine (ME-2) for the source apportionment: ME-2 application to aerosol mass spectrometer data. Atmos. Meas. Tech. 6, 3649–3661. https://doi.org/10.5194/amt-6-3649-2013.

Chakraborty, A., Gupta, T., 2010. Chemical characterization and source apportionment of submicron (PM_1) aerosol in Kanpur region, India. Aerosol Air Qual. Res. 10, 433–445. https://doi.org/10.4209/aaqr.2009.11.0071.

Chandra, S., Kulshrestha, M.J., Singh, R., 2014. Temporal variation and concentration weighted trajectory analysis of lead in PM_{10} aerosols at a site in Central Delhi, India. Int. J. Atmos. Sci. 2014, 1–8. https://doi.org/10.1155/2014/323040.

Chang, Y., Huang, K., Xie, M., Deng, C., Zou, Z., Liu, S., Zhang, Y., 2018. First long-term and near real-time measurement of trace elements in China's urban atmosphere: temporal variability, source apportionment and precipitation effect. Atmos. Chem. Phys. 18, 11793–11812. https://doi.org/10.5194/acp-18-11793-2018.

Cheng, Y., Lee, S., Gu, Z., Ho, K., Zhang, Y., Huang, Y., Chow, J.C., Watson, J.G., Cao, J., Zhang, R., 2015. $PM_{2.5}$ and $PM_{10\text{-}2.5}$ chemical composition and source apportionment near a Hong Kong roadway. Partic 18, 96–104. https://doi.org/10.1016/j.partic.2013.10.003.

Chiou, K.Y., Manuel, O.K., 1986. Tellurium and selenium in aerosols. Environ. Sci. Technol. 20, 987–991. https://doi.org/10.1021/es00152a003.

Daellenbach, K.R., Bozzetti, C., Křepelová, A., Canonaco, F., Wolf, R., Zotter, P., Fermo, P., Crippa, M., Slowik, J.G., Sosedova, Y., Zhang, Y., Huang, R.J., Poulain, L., Szidat, S., Baltensperger, U., El Haddad, I., Prévôt, A.S.H., 2016. Characterization and source apportionment of organic aerosol using offline aerosol mass spectrometry. Atmos. Meas. Tech. 9, 23–39. https://doi.org/10.5194/amt-9-23-2016.

Daellenbach, K.R., Stefenelli, G., Bozzetti, C., Vlachou, A., Fermo, P., Gonzalez, R., Piazzalunga, A., Colombi, C., Canonaco, F., Hueglin, C., Kasper-Giebl, A., Jaffrezo, J.-L., Bianchi, F., Slowik, J.G., Baltensperger, U., El-Haddad, I., Prévôt, A.S.H., 2017. Long-term chemical analysis and organic aerosol source apportionment at nine sites in Central Europe: source identification and uncertainty assessment. Atmos. Chem. Phys. 17, 13265–13282. https://doi.org/10.5194/acp-17-13265-2017.

Dall'Osto, M., Querol, X., Amato, F., Karanasiou, A., Lucarelli, F., Nava, S., Calzolai, G., Chiari, M., 2013. Hourly elemental concentrations in $PM_{2.5}$ aerosols sampled simultaneously at urban background and road site during SAPUSS – diurnal variations and PMF receptor modelling. Atmos. Chem. Phys. 13, 4375–4392. https://doi.org/10.5194/acp-13-4375-2013.

Davison, A.C., Hinkley, D.V., 1997. Bootstrap Methods and Their Application. Cambridge University Press https://doi.org/10.1017/CBO9780511802843.

DeCarlo, P.F., Kimmel, J.R., Trimborn, A., Northway, M.J., Jayne, J.T., Aiken, A.C., Gonin, M., Fuhrer, K., Horvath, T., Docherty, K.S., Worsnop, D.R., Jimenez, J.L., 2006. Field-deployable, high-resolution, time-of-flight aerosol mass spectrometer. Anal. Chem. 78, 8281–8289. https://doi.org/10.1029/2001jd001213.

Delhi Police, 2015. Restriction on the movement of LGV and HGV/MGV vehicles. Available at:. https://delhitrafficpolice.nic.in/sites/default/files/uploads/2015/02/notification-2.pdf.

Draxler, R., Stunder, B., Rolph, G., Stein, A., Taylor, A., 2018. HYSPLIT4 User's Guide. Air Resources Laboratory, Silver Spring, MD https://www.arl.noaa.gov/documents/reports/hysplit_user_guide.pdf.

Draxler, R.R., 1999. HYSPLIT4 user's guide. NOAA Tech. Memo, ERL ARL-230. NOAA Air Resources Laboratory, Silver Spring, MD https://www.arl.noaa.gov/wp_arl/wp-content/uploads/documents/reports/arl-230.pdf.

Duan, J., Tan, J., 2013. Atmospheric heavy metals and arsenic in China: situation, sources and control policies. Atmos. Environ. 74, 93–101. https://doi.org/10.1016/j.atmosenv.2013.03.031.

Dumka, U.C., Tiwari, S., Kaskaoutis, D.G., Soni, V.K., Safai, P.D., Attri, S.D., 2019. Aerosol and pollutant characteristics in Delhi during a winter research campaign. Environ. Sci. Pollut. Res. Int. 26, 3771–3794. https://doi.org/10.1007/s11356-018-3885-y.

Economic Survey of Delhi 2018–19: Planning Department, Government of NCT of Delhi. http://delhiplanning.nic.in/sites/default/files/Final%20Economy%20survey%20English.pdf.

Fomba, K.W., Müller, K., van Pinxteren, D., Herrmann, H., 2013. Aerosol size-resolved trace metal composition in remote northern tropical Atlantic marine environment: case study Cape Verde islands. Atmos. Chem. Phys. 13, 4801–4814. https://doi.org/10.5194/acp-13-4801-2013.

Frazzoli, C., Orisakwe, O.E., Dragone, R., Mantovani, A., 2010. Diagnostic health risk assessment of electronic waste on the general population in developing countries' scenarios. Environ. Impact Assess. Rev. 30, 388–399. https://doi.org/10.1016/j.eiar.2009.12.004.

Fröhlich, R., Cubison, M.J., Slowik, J.G., Bukowiecki, N., Prévôt, A.S.H., Baltensperger, U., Schneider, J., Kimmel, J.R., Gonin, M., Rohner, U., Worsnop, D.R., Jayne, J.T., 2013. The ToF-ACSM: a portable aerosol chemical speciation monitor with TOFMS detection. Atmos. Meas. Tech. 6, 3225–3241. https://doi.org/10.5194/amt-6-3225-2013.

Furger, M., Minguillón, M.C., Yadav, V., Slowik, J.G., Hüglin, C., Fröhlich, R., Petterson, K., Baltensperger, U., Prévôt, A.S.H., 2017. Elemental composition of ambient aerosols measured with high temporal resolution using an online XRF spectrometer. Atmos. Meas. Tech. 10, 2061–2076. https://doi.org/10.5194/amt-10-2061-2017.

Furger, M., Rai, P., Slowik, J.G., Cao, J., Visser, S., Baltensperger, U., Prévôt, A.S.H., 2020. Automated alternating sampling of PM_{10} and $PM_{2.5}$ with an online XRF spectrometer. Atmos. Environ.: X 5, 100065. https://doi.org/10.1016/j.aeaoa.2020.100065.

Gani, S., Bhandari, S., Seraj, S., Wang, D.S., Patel, K., Soni, P., Arub, Z., Habib, G., Hildebrandt Ruiz, L., Apte, J.S., 2019. Submicron aerosol composition in the world's most polluted megacity: the Delhi aerosol supersite study. Atmos. Chem. Phys. 19, 6843–6859. https://doi.org/10.5194/acp-19-6843-2019.

Gietl, J.K., Lawrence, R., Thorpe, A.J., Harrison, R.M., 2010. Identification of brake wear particles and derivation of a quantitative tracer for brake dust at a major road. Atmos. Environ. 44, 141–146. https://doi.org/10.1016/j.atmosenv.2009.10.016.

Gollakota, A.R.K., Volli, V., Shu, C.-M., 2019. Progressive utilisation prospects of coal fly ash: a review. Sci. Total Environ. 672, 951–989. https://doi.org/10.1016/j.scitotenv.2019.03.337.

Gupta, A.K., Karar, K., Srivastava, A., 2007. Chemical mass balance source apportionment of PM_{10} and TSP in residential and industrial sites of an urban region of Kolkata, India. J. Hazard. Mater. 142, 279–287. https://doi.org/10.1016/j.jhazmat.2006.08.013.

Guttikunda, S.K., Calori, G., 2013. A GIS based emissions inventory at 1 km × 1 km spatial resolution for air pollution analysis in Delhi, India. Atmos. Environ. 67, 101–111. https://doi.org/10.1016/j.atmosenv.2012.10.040.

Guttikunda, S.K., Gurjar, B.R., 2012. Role of meteorology in seasonality of air pollution in megacity Delhi, India. Environ. Monit. Assess. 184, 3199–3211. https://doi.org/10.1007/s10661-011-2182-8.

Hao, Y., Meng, X., Yu, X., Lei, M., Li, W., Yang, W., Shi, F., Xie, S., 2020. Quantification of primary and secondary sources to $PM_{2.5}$ using an improved source regional apportionment method in an industrial city, China. Sci. Total Environ. 706, 135715. https://doi.org/10.1016/j.scitotenv.2019.135715.

Hinneburg, D., Renner, E., Wolke, R., 2009. Formation of secondary inorganic aerosols by power plant emissions exhausted through cooling towers in Saxony. Environ. Sci. Pollut. Res. Int. 16, 25–35. https://doi.org/10.1007/s11356-008-0081-5.

Hooper, L.G., Kaufman, J.D., 2018. Ambient air pollution and clinical implications for susceptible populations. Ann. Am. Thorac. Soc. 15, S64–S68. https://doi.org/10.1513/AnnalsATS.201707-574MG.

Hsu, C.Y., Holsen, T.M., Hopke, P., 2003. Comparison of hybrid receptor models to locate PCB sources in Chicago. Atmos. Environ. 37, 545–562. https://doi.org/10.1016/S1352-2310(02)00886-5.

Husain, L., Ghauri, B., Yang, K., Khan, A.R., Rattigan, O.V., 2004. Application of the SO_4^{2-}/Se tracer technique to study SO_2 oxidation in cloud and fog on a time scale of minutes. Chemos 54, 177–183. https://doi.org/10.1016/S0045-6535(03)00531-9.

Jaiprakash, Singhai, A., Habib, G., Raman, R.S., Gupta, T., 2017. Chemical characterization of $PM_{1.0}$ aerosol in Delhi and source apportionment using positive matrix factorization. Environ. Sci. Pollut. Res. Int. 24, 445–462. https://doi.org/10.1007/s11356-016-7708-8.

Jaiprakash, Lohia, T., Mandariya, A.K., Habib, G., Gupta, T., Gupta, S.K., 2018. Chemical characterization and quantitative assessment of source-specific health risk of trace metals in $PM_{1.0}$ at a road site of Delhi, India. Environ. Sci. Pollut. Res. Int. 25, 8747–8764. https://doi.org/10.1007/s11356-017-1174-9.

Jayarathne, T., Stockwell, C.E., Bhave, P.V., Praveen, P.S., Rathnayake, C.M., Islam, M.R., Panday, A.K., Adhikari, S., Maharjan, R., Goetz, J.D., DeCarlo, P.F., Saikawa, E., Yokelson, R.J., Stone, E.A., 2018. Nepal ambient monitoring and source testing experiment (NAMaSTE): emissions of particulate matter from wood- and dung-fueled cooking fires, garbage and crop residue burning, brick kilns, and other sources. Atmos. Chem. Phys. 18, 2259–2286. https://doi.org/10.5194/acp-18-2259-2018.

Julander, A., Lundgren, L., Skare, L., Grander, M., Palm, B., Vahter, M., Liden, C., 2014. Formal recycling of e-waste leads to increased exposure to toxic metals: an occupational exposure study from Sweden. Environ. Int. 73, 243–251. https://doi.org/10.1016/j.envint.2014.07.006.

Karar, K., Gupta, A.K., Kumar, A., Biswas, A.K., 2006. Characterization and identification of the sources of chromium, zinc, lead, cadmium, nickel, manganese and iron in PM_{10} particulates at the two sites of Kolkata, India. Environ. Monit. Assess. 120, 347–360. https://doi.org/10.1007/s10661-005-9067-7.

Kennedy, P., Gadd, J., 2003. Preliminary Examination of Trace Elements in Tyres, Brake Pads, and Road Bitumen in New Zealand. Kingett Mitchell Ltd https://rcaforum.org.nz/sites/public_files/documents/stormwater-organiccompounds2.pdf.

Khillare, P.S., Sarkar, S., 2012. Airborne inhalable metals in residential areas of Delhi, India: distribution, source apportionment and health risks. Atmos. Pollut. Res. 3, 46–54. https://doi.org/10.5094/apr.2012.004.

Khodeir, M., Shamy, M., Alghamdi, M., Zhong, M., Sun, H., Costa, M., Chen, L.-C., Maciejczyk, P., 2012. Source apportionment and elemental composition of $PM_{2.5}$ and PM_{10} in Jeddah City, Saudi Arabia. Atmos. Pollut. Res. 3, 331–340. https://doi.org/10.5094/apr.2012.037.

Kirillova, E.N., Andersson, A., Tiwari, S., Srivastava, A.K., Bisht, D.S., Gustafsson, Ö., 2014. Water-soluble organic carbon aerosols during a full New Delhi winter: isotope-based source apportionment and optical properties. J. Geophys. Res. Atmos. 119, 3476–3485. https://doi.org/10.1002/2013jd020041.

Kothai, P., Saradhi, I.V., Pandit, G.G., Markwitz, A., Puranik, V.D., 2011. Chemical characterization and source identification of particulate matter at an urban site of Navi Mumbai, India. Aerosol Air Qual. Res. 11, 560–569. https://doi.org/10.4209/aaqr.2011.02.0017.

Kumar, S., Aggarwal, S.G., Gupta, P.K., Kawamura, K., 2015. Investigation of the tracers for plastic-enriched waste burning aerosols. Atmos. Environ. 108, 49–58. https://doi.org/10.1016/j.atmosenv.2015.02.066.

Kumar, S., Aggarwal, S.G., Sarangi, B., Malherbe, J., Barre, J.P.G., Berail, S., Séby, F., Donard, O.F.X., 2018. Understanding the influence of open-waste burning on urban aerosols using metal tracers and lead isotopic composition. Aerosol Air Qual. Res. 18, 2433–2446. https://doi.org/10.4209/aaqr.2017.11.0510.

Li, G., Lei, W., Bei, N., Molina, L.T., 2012. Contribution of garbage burning to chloride and $PM_{2.5}$ in Mexico City. Atmos. Chem. Phys. 12, 8751–8761. https://doi.org/10.5194/acp-12-8751-2012.

Li, M., Li, L., Strielkowski, W., 2019. The impact of urbanization and industrialization on energy security: a case study of China. Energies 12. https://doi.org/10.3390/en12112194.

Lucarelli, F., Calzolai, G., Chiari, M., Nava, S., Carraresi, L., 2018. Study of atmospheric aerosols by IBA techniques: the LABEC experience. Nuclear Instr. Methods Phys. Res. Sect. B: Beam Interac. Mater. Atmos. 417, 121–127. https://doi.org/10.1016/j.nimb.2017.07.034.

Majewski, G., Rogula-Kozlowska, W., 2016. The elemental composition and origin of fine ambient particles in the largest Polish conurbation: first results from the short-term winter campaign. Theo. Appl. Climat. 125, 79–92. https://doi.org/10.1007/s00704-015-1494-y.

Matawle, J.L., Pervez, S., Dewangan, S., Shrivastava, A., Tiwari, S., Pant, P., Deb, M.K., Pervez, Y., 2015. Characterization of $PM_{2.5}$ source profiles for traffic and dust sources in Raipur, India. Aerosol Air Qual. Res. 15, 2537–2548. https://doi.org/10.4209/aaqr.2015.04.0222.

Morawska, L., Zhang, J., 2002. Combustion sources of particles: 1. Health relevance and source signatures. Chemos 49, 1045–1058. https://doi.org/10.1016/s0045-6535(02)00241-2.

Ntziachristos, L., Ning, Z., Geller, M.D., Sheesley, R.J., Schauer, J.J., Sioutas, C., 2007. Fine, ultrafine and nanoparticle trace element compositions near a major freeway with a high heavy-duty diesel fraction. Atmos. Environ. 41, 5684–5696. https://doi.org/10.1016/j.atmosenv.2007.02.043.

Owoade, K.O., Hopke, P.K., Olise, F.S., Ogundele, L.T., Fawole, O.G., Olaniyi, B.H., Jegede, O.O., Ayoola, M.A., Bashiru, M.I., 2015. Chemical compositions and source identification of particulate matter ($PM_{2.5}$ and $PM_{2.5-10}$) from a scrap iron and steel smelting industry along the Ife–Ibadan highway, Nigeria. Atmos. Pollut. Res. 6, 107–119. https://doi.org/10.5094/apr.2015.013.

Paatero, P., 1999. The multilinear engine—a table-driven, least squares program for solving multilinear problems, including the *n*-way parallel factor analysis model. J. Comput. Graph. Stat. 8, 854–888. https://doi.org/10.1080/10618600.1999.10474853.

Paatero, P., Hopke, P.K., 2003. Discarding or downweighting high-noise variables in factor analytic models. Anal. Chim. Acta 490, 277–289. https://doi.org/10.1016/s0003-2670(02)01643-4.

Paatero, P., Tapper, U., 1994. Positive matrix factorization: a non-negative factor model with optimal utilization of error-estimates of data values. Environmet 5, 111–126. https://doi.org/10.1002/env.3170050203.

Paatero, P., Eberly, S., Brown, S.G., Norris, G.A., 2014. Methods for estimating uncertainty in factor analytic solutions. Atmos. Meas. Tech. 7, 781–797. https://doi.org/10.5194/amt-7-781-2014.

Pant, P., Harrison, R.M., 2012. Critical review of receptor modelling for particulate matter: a case study of India. Atmos. Environ. 49, 1–12. https://doi.org/10.1016/j.atmosenv.2011.11.060.

Pant, P., Harrison, R.M., 2013. Estimation of the contribution of road traffic emissions to particulate matter concentrations from field measurements: a review. Atmos. Environ. 77, 78–97. https://doi.org/10.1016/j.atmosenv.2013.04.028.

Pant, P., Baker, S.J., Shukla, A., Maikawa, C., Godri Pollitt, K.J., Harrison, R.M., 2015a. The PM_{10} fraction of road dust in the UK and India: characterization, source profiles and oxidative potential. Sci. Total Environ. 530–531, 445–452. https://doi.org/10.1016/j.scitotenv.2015.05.084.

Pant, P., Shukla, A., Kohl, S.D., Chow, J.C., Watson, J.G., Harrison, R.M., 2015b. Characterization of ambient $PM_{2.5}$ at a pollution hotspot in New Delhi, India and inference of sources. Atmos. Environ. 109, 178–189. https://doi.org/10.1016/j.atmosenv.2015.02.074.

Park, S.S., Cho, S.Y., Jo, M.R., Gong, B.J., Park, J.S., Lee, S.J., 2014. Field evaluation of a near-real time elemental monitor and identification of element sources observed at an air monitoring supersite in Korea. Atmos. Pollut. Res. 5, 119–128. https://doi.org/10.5094/apr.2014.015.

Patil, R.S., Kumar, R., Menon, R., Shah, M.K., Sethi, V., 2013. Development of particulate matter speciation profiles for major sources in six cities in India. Atmos. Res. 132–133, 1–11. https://doi.org/10.1016/j.atmosres.2013.04.012.

Petit, J.-E., Favez, O., Albinet, A., Canonaco, F., 2017. A user-friendly tool for comprehensive evaluation of the geographical origins of atmospheric pollution: wind and trajectory analyses. Environ. Model. Softw. 88, 183–187. https://doi.org/10.1016/j.envsoft.2016.11.022.

Phillips-Smith, C., Jeong, C.-H., Healy, R.M., Dabek-Zlotorzynska, E., Celo, V., Brook, J.R., Evans, G., 2017. Sources of particulate matter components in the Athabasca oil sands region: investigation through a comparison of trace element measurement methodologies. Atmos. Chem. Phys. 17, 9435–9449. https://doi.org/10.5194/acp-17-9435-2017.

Pipalatkar, P., Khaparde, V.V., Gajghate, D.G., Bawase, M.A., 2014. Source apportionment of $PM_{2.5}$ using a CMB model for a centrally located Indian city. Aerosol Air Qual. Res. 14, 1089–1099. https://doi.org/10.4209/aaqr.2013.04.0130.

Polissar, A.V., Hopke, P.K., Paatero, P., Malm, W.C., Sisler, J.F., 1998. Atmospheric aerosol over Alaska: 2. Elemental composition and sources. J. Geophys. Res. Atmos. 103, 19045–19057. https://doi.org/10.1029/98jd01212.

Puthussery, J.V., Singh, A., Rai, P., Bhattu, D., Kumar, V., Vats, P., Furger, M., Rastogi, N., Slowik, J.G., Ganguly, D., Prévôt, A.S.H., Tripathi, S.N., Verma, V., 2020. Real-time measurements of $PM_{2.5}$ oxidative potential using a dithiothreitol assay in Delhi, India. Environ. Sci. Technol. Lett. https://doi.org/10.1021/acs.estlett.0c00342.

Rai, P., Furger, M., Slowik, J., Canonaco, F., Fröhlich, R., Hüglin, C., Minguillón, M.C., Petterson, K., Baltensperger, U., Prévôt, A.S.H., 2020. Source apportionment of highly time-resolved elements during a firework episode from a rural freeway site in Switzerland. Atmos. Chem. Phys. 20, 1657–1674. https://doi.org/10.5194/acp-20-1657-2020.

Reff, A., Eberly, S.I., Bhave, P.V., 2007. Receptor modeling of ambient particulate matter data using positive matrix factorization: review of existing methods. 57, 146–154. https://doi.org/10.1080/10473289.2007.10465319.

Richard, A., Bukowiecki, N., Lienemann, P., Furger, M., Fierz, M., Minguillón, M.C., Weideli, B., Figi, R., Flechsig, U., Appel, K., Prévôt, A.S.H., Baltensperger, U., 2010. Quantitative sampling and analysis of trace elements in atmospheric aerosols: impactor characterization and synchrotron-XRF mass calibration. Atmos. Meas. Tech. 3, 1473–1485. https://doi.org/10.5194/amt-3-1473-2010.

Rudnick, R., Gao, S., 2003. Composition of the continental crust. In: Rudnick, E. (Ed.), The Crust. 3. Elsevier Science, Philadelphia, pp. 1–56 Book Section 2.

Sharma, S.K., Mandal, T.K., Saxena, M., Rashmi Sharma, A., Datta, A., Saud, T., 2014. Variation of OC, EC, WSIC and trace metals of PM10 in Delhi, India. J. Atmos. Solar Terrest. Phys. 113, 10–22. https://doi.org/10.1016/j.jastp.2014.02.008.

Sharma, S.K., Mandal, T.K., Jain, S., Saraswati Sharma, A., Saxena, M., 2016. Source apportionment of PM2.5 in Delhi, India using PMF model. Bull. Environ. Contam. Toxicol. 97, 286–293. https://doi.org/10.1007/s00128-016-1836-1.

Simoneit, B.R.T., Schauer, J.J., Nolte, C.G., Oros, D.R., Elias, V.O., Fraser, M.P., Rogge, W.F., Cass, G.R., 1999. Levoglucosan, a tracer for cellulose in biomass burning and atmospheric particles. Atmos. Environ. 33, 173–182. https://doi.org/10.1016/S1352-2310(98)00145-9.

Song, F., Gao, Y., 2011. Size distributions of trace elements associated with ambient particular matter in the affinity of a major highway in the New Jersey–New York metropolitan area. Atmos. Environ. 45, 6714–6723. https://doi.org/10.1016/j.atmosenv.2011.08.031.

Srimuruganandam, B., Nagendra, S.M.S., 2012. Source characterization of PM_{10} and $PM_{2.5}$ mass using a chemical mass balance model at urban roadside. Sci. Total Environ. 433, 8–19. https://doi.org/10.1016/j.scitotenv.2012.05.082.

Stefenelli, G., Pospisilova, V., Lopez-Hilfiker, F.D., Daellenbach, K.R., Hüglin, C., Tong, Y., Baltensperger, U., Prévôt, A.S.H., Slowik, J.G., 2019. Organic aerosol source apportionment in Zurich using an extractive electrospray ionization time-of-flight mass spectrometer (EESI-TOF-MS) – part 1: biogenic influences and day–night chemistry in summer. Atmos. Chem. Phys. 19, 14825–14848. https://doi.org/10.5194/acp-19-14825-2019.

Stein, A.F., Draxler, R.R., Rolph, G.D., Stunder, B.J.B., Cohen, M.D., Ngan, F., 2015. NOAA's HYSPLIT atmospheric transport and dispersion modeling system. Bull. Am. Meteorol. Soc. 96, 2059–2077. https://doi.org/10.1175/bams-d-14-00110.1.

Sturtz, T.M., Adar, S.D., Gould, T., Larson, T.V., 2014. Constrained source apportionment of coarse particulate matter and selected trace elements in three cities from the multi-ethnic study of atherosclerosis. Atmos. Environ. 84, 65–77. https://doi.org/10.1016/j.atmosenv.2013.11.031.

Sun, J., Shen, Z., Zhang, L., Lei, Y., Gong, X., Zhang, Q., Zhang, T., Xu, H., Cui, S., Wang, Q., Cao, J., Tao, J., Zhang, N., Zhang, R., 2019. Chemical source profiles of urban fugitive dust $PM_{2.5}$ samples from 21 cities across China. Sci. Total Environ. 649, 1045–1053. https://doi.org/10.1016/j.scitotenv.2018.08.374.

Syakur, M.A., Khotimah, B.K., Rochman, E.M.S., Satoto, B.D., 2018. Integration *K*-means clustering method and elbow method for identification of the best customer profile cluster. IOP Conference Series: Materials Science and Engineering 336. https://doi.org/10.1088/1757-899x/336/1/012017.

Thammadi, S.P.D., Pisini, S.K., Shukla, S.K., 2018. Estimation of $PM_{2.5}$ emissions and source apportionment using receptor and dispersion models. Int. Earth Energy Environ. Sci. 11.0 (7). https://doi.org/10.5281/zenodo.1340436.

Tian, S.L., Pan, Y.P., Wang, Y.S., 2016. Size-resolved source apportionment of particulate matter in urban Beijing during haze and non-haze episodes. Atmos. Chem. Phys. 16, 1–19. https://doi.org/10.5194/acp-16-1-2016.

Tiwari, S., Srivastava, A.K., Bisht, D.S., Parmita, P., Srivastava, M.K., Attri, S.D., 2013. Diurnal and seasonal variations of black carbon and $PM_{2.5}$ over New Delhi, India: influence of meteorology. Atmos. Res. 125–126, 50–62. https://doi.org/10.1016/j.atmosres.2013.01.011.

Tremper, A.H., Font, A., Priestman, M., Hamad, S.H., Chung, T.-C., Pribadi, A., Brown, R.J.C., Goddard, S.L., Grassineau, N., Petterson, K., Kelly, F.J., Green, D.C., 2018. Field and laboratory evaluation of a high time resolution X-ray fluorescence instrument for determining the elemental composition of ambient aerosols. Atmos. Meas. Tech. 11, 3541–3557. https://doi.org/10.5194/amt-11-3541-2018.

USEPA, 2019. Regional screening levels (RSLs). www.epa.gov/risk/regional-screening-levels-rsls-generic-tables.

Van Damme, M., Clarisse, L., Whitburn, S., Hadji-Lazaro, J., Hurtmans, D., Clerbaux, C., Coheur, P.F., 2018. Industrial and agricultural ammonia point sources exposed. Nature 564, 99–103. https://doi.org/10.1038/s41586-018-0747-1.

Viana, M., Kuhlbusch, T.A.J., Querol, X., Alastuey, A., Harrison, R.M., Hopke, P.K., Winiwarter, W., Vallius, M., Szidat, S., Prévôt, A.S.H., Hueglin, C., Bloemen, H., Wåhlin, P., Vecchi, R., Miranda, A.I., Kasper-Giebl, A., Maenhaut, W., Hitzenberger, R., 2008. Source apportionment of particulate matter in Europe: a review of methods and results. J. Aerosol Sci. 39, 827–849. https://doi.org/10.1016/j.jaerosci.2008.05.007.

Viana, M., Reche, C., Amato, F., Alastuey, A., Querol, X., Moreno, T., Lucarelli, F., Nava, S., Calzolai, G., Chiari, M., Rico, M., 2013. Evidence of biomass burning aerosols in the Barcelona urban environment during winter time. Atmos. Environ. 72, 81–88. https://doi.org/10.1016/j.atmosenv.2013.02.031.

Vincent, K., Passant, N., 2006. Assessment of heavy metal concentrations in the United Kingdom. Report to the Department for Environment, Food and Rural Affairs, Welsh Assembly Government, the Scottish Executive and the Department of the Environment for Northern Ireland. AEAT/ENV/R/2013/Issue 1. AEA Technology https://uk-air.defra.gov.uk/assets/documents/reports/cat16/0604041205_heavy_metal_issue1_final.pdf.

Visser, S., Slowik, J.G., Furger, M., Zotter, P., Bukowiecki, N., Canonaco, F., Flechsig, U., Appel, K., Green, D.C., Tremper, A.H., Young, D.E., Williams, P.I., Allan, J.D., Coe, H., Williams, L.R., Mohr, C., Xu, L., Ng, N.L., Nemitz, E., Barlow, J.F., Halios, C.H., Fleming, Z.L., Baltensperger, U., Prévôt, A.S.H., 2015. Advanced source apportionment of size-resolved trace elements at multiple sites in London during winter. Atmos. Chem. Phys. 15, 11291–11309. https://doi.org/10.5194/acp-15-11291-2015.

Vlachou, A., Daellenbach, K.R., Bozzetti, C., Chazeau, B., Salazar, G.A., Szidat, S., Jaffrezo, J.-L., Hueglin, C., Baltensperger, U., El Haddad, I., Prévôt, A.S.H., 2018. Advanced source apportionment of carbonaceous aerosols by coupling offline AMS and radiocarbon size-segregated measurements over a nearly 2-year period. Atmos. Chem. Phys. 18, 6187–6206. https://doi.org/10.5194/acp-18-6187-2018.

Waked, A., Favez, O., Alleman, L.Y., Piot, C., Petit, J.E., Delaunay, T., Verlinden, E., Golly, B., Besombes, J.L., Jaffrezo, J.L., Leoz-Garziandia, E., 2014. Source apportionment of PM_{10} in a north-western Europe regional urban background site (Lens, France) using positive matrix factorization and including primary biogenic emissions. Atmos. Chem. Phys. 14, 3325–3346. https://doi.org/10.5194/acp-14-3325-2014.

Wang, G., Kawamura, K., Cheng, C., Li, J., Cao, J., Zhang, R., Zhang, T., Liu, S., Zhao, Z., 2012. Molecular distribution and stable carbon isotopic composition of dicarboxylic acids, ketocarboxylic acids, and alpha-dicarbonyls in size-resolved atmospheric particles from Xi'an City, China. Environ. Sci. Technol. 46, 4783–4791. https://doi.org/10.1021/es204322c.

Wang, L., Slowik, J.G., Tripathi, N., Bhattu, D., Rai, P., Kumar, V., Vats, P., Baltensperger, U., Ganguly, D., Sahu, L.K., Tripathi, S.N., Prévôt, A.S.H., 2020. Source characterization of volatile organic compounds measured by PTR-ToF-MS in Delhi, India. Atmos. Chem. Phys. Discuss. https://doi.org/10.5194/acp-2020-11.

Warner, J.X., Dickerson, R.R., Wei, Z., Strow, L.L., Wang, Y., Liang, Q., 2017. Increased atmospheric ammonia over the world's major agricultural areas detected from space. Geophys. Res. Lett. 44, 2875–2884. https://doi.org/10.1002/2016GL072305.

Weber, S., Salameh, D., Albinet, A., Alleman, L.Y., Waked, A., Besombes, J.-L., Jacob, V., Guillaud, G., Meshbah, B., Rocq, B., Hulin, A., Dominik-Sègue, M., Chrétien, E., Jaffrezo, J.-L., Favez, O., 2019. Comparison of PM_{10} sources profiles at 15 French

sites using a harmonized constrained positive matrix factorization approach. Atmos 10, 310. https://doi.org/10.3390/atmos10060310.
Whiley, A.J., 2011. Copper and Zinc Loading Associated with Automotive Brake-Pad and Tire Wear. Water Quality Program Washington State Department of Ecology Olympia, Washington https://fortress.wa.gov/ecy/publications/documents/1110087.pdf.
White, S.J.O., Hemond, H.F., 2019. Emerging investigator series: atmospheric cycling of indium in the northeastern United States. Environ Sci Process Impacts 21, 623–634. https://doi.org/10.1039/c8em00485d.
Wong, M.H., Wu, S.C., Deng, W.J., Yu, X.Z., Luo, Q., Leung, A.O., Wong, C.S., Luksemburg, W.J., Wong, A.S., 2007. Export of toxic chemicals - a review of the case of uncontrolled electronic-waste recycling. Environ. Pollut. 149, 131–140. https://doi.org/10.1016/j.envpol.2007.01.044.
Zhang, Y.L., Huang, R.J., El Haddad, I., Ho, K.F., Cao, J.J., Han, Y., Zotter, P., Bozzetti, C., Daellenbach, K.R., Canonaco, F., Slowik, J.G., Salazar, G., Schwikowski, M., Schnelle-Kreis, J., Abbaszade, G., Zimmermann, R., Baltensperger, U., Prévôt, A.S.H., Szidat, S., 2015. Fossil vs. non-fossil sources of fine carbonaceous aerosols in four Chinese cities during the extreme winter haze episode of 2013. Atmos. Chem. Phys. 15, 1299–1312. https://doi.org/10.5194/acp-15-1299-2015.